Using the Artificial Tracer e90 to Examine Present and Future UTLS Tracer Transport in WACCM

MARTA ABALOS, WILLIAM J. RANDEL, DOUGLAS E. KINNISON, AND ROLANDO R. GARCIA

National Center for Atmospheric Research, Boulder, Colorado

(Manuscript received 26 April 2017, in final form 20 July 2017)

ABSTRACT

Large-scale tracer transport in the upper troposphere and lower stratosphere (UTLS) is investigated using simulations of the Whole Atmosphere Community Climate Model (WACCM) over the period 1955–2099. The analyses are based on e90, an artificial passive tracer with constant emissions and atmospheric loss rates. The separate contributions of advection by the residual circulation, eddy mixing, and subgrid convection to total transport are explicitly evaluated. The results highlight distinct large-scale transport regimes in the tropics, characterized by efficient vertical tracer transport, and the extratropics, dominated by isentropic mixing. One novel result is the important role of vertical eddy mixing in the tropical upper troposphere. It is shown that interannual variability in e90 is largely driven by El Niño–Southern Oscillation and the quasi-biennial oscillation. The long-term trends emphasize a strong impact of a rising tropopause with climate change on UTLS dynamics and tracer transport. The analyses directly attribute the e90 trends to changes in the different transport components. Stronger residual circulation in the future leads to increased tracer concentrations in the tropical lower stratosphere. Enhanced eddy mixing increases e90 in the extratropical lowermost stratosphere, linked to an upward shift of wave dissipation tied to the tropopause rise. In the troposphere, reduced concentrations in the future are due to weaker convective transport out of the boundary layer and weaker extratropical isentropic eddy mixing.

1. Introduction

The distribution and variability of chemical compounds in the upper troposphere and lower stratosphere (UTLS) play a particularly important radiative role in the climate system (e.g., Forster and Shine 1997; Forster and Shine 2002). Because of the very different chemical composition of the troposphere and the stratosphere and the resulting strong tracer gradients in this transition region, transport processes are major drivers of variability in the UTLS composition (Holton et al. 1995). Observational and modeling studies have shown large intraseasonal to interannual variability in radiatively active tracers in this region, such as water vapor and ozone, associated with variability in transport (e.g., Mote et al. 1996; Randel et al. 2004; Randel et al. 2007; Abalos et al. 2012; Ploeger et al. 2012). In addition, long-term trends in UTLS composition driven by changes in transport are expected as the climate warms as a result of increasing anthropogenic emissions. For instance, concentrations of tropospheric ozone could increase because of enhanced stratosphere-to-troposphere transport in the future (e.g., Neu et al. 2014; Banerjee et al. 2016). Predicted changes in the stratospheric circulation can modify the amount of water vapor concentrations in the lower stratosphere, with potentially important impacts for global climate (e.g., Solomon et al. 2010; Maycock et al. 2014). Predicting the future evolution of chemical species implies not only correctly representing transport but also the chemical mechanisms. Indeed, for chemical species with time-varying sources, changes in circulation can play a secondary role on the long-term trends (Garcia et al. 2007). Moreover, feedbacks between chemistry, radiation, and dynamics make attributing model trends challenging, especially since the exact role of these feedbacks on climate is still not well understood (Nowack et al. 2014; Marsh et al. 2016).

This complexity motivates the use of artificial tracers to study tracer transport in isolation from chemical processes and their two-way interactions with dynamics. This approach has been widely exploited to investigate

Corresponding author: Marta Abalos, mabalosa@ucm.es

DOI: 10.1175/JAS-D-17-0135.1

the characteristics of large-scale transport in general circulation models. In particular, a number of studies have derived the statistics of transport (sometimes referred to as the transport climate) from the dispersion of passive tracer pulses emitted at the surface, using the Green function as a propagator (e.g., Mahlman and Moxim 1978; Plumb and Mahlman 1987; Holzer 1999; Bowman and Carrie 2002; Erukhimova and Bowman 2006). Stratospheric age of air, which can be thought as a clock tracer initialized at the tropopause, has been extensively used to evaluate transport time scales in the stratosphere (e.g., Hall and Plumb 1994; Waugh and Hall 2002). In the present work, the artificial tracer e90 is used to examine UTLS transport. This tracer was introduced by Prather et al. (2011) with the aim of defining a tropopause that effectively separates stratospheric from tropospheric air from a chemical composition perspective. It has been used in recent studies of stratosphere–troposphere exchange both as an accurate tropopause definition and as a UTLS passive tracer (e.g., Hsu and Prather 2014; Yang et al. 2016; Randel et al. 2016; Pan et al. 2016). The tracer e90 is emitted uniformly at the surface (i.e., an identical e90 flux is imposed at every grid point in the lower boundary of the model) and has an *e*-folding lifetime of 90 days everywhere in the atmosphere (i.e., the loss rate is given by the local concentration of e90 divided by 90 days). This lifetime is long enough to allow for the tracer to become fairly well mixed throughout the troposphere but short with respect to the transport time scales in the stratosphere. This results in sharp e90 gradients across the tropopause, similar to those exhibited by real tracers such as ozone or carbon monoxide (CO). The homogeneous and constant emissions and loss allow us to extract general conclusions on large-scale transport characteristics. In particular, long-term trends in this tracer can be attributed to changes in transport alone, independently of changes in emissions or chemical processes.

Zonal-mean tracer transport in the transformed Eulerian mean (TEM) framework can be conveniently divided into a component due to advection by the mean residual circulation plus an eddy transport component, linked to rapid stirring and two-way mixing of air masses (e.g., Andrews et al. 1987). This separation provides information on the contribution of each transport process to the mean tracer distribution and the total transport time scales in different regions (e.g., Randel et al. 1994; Ploeger et al. 2015; Ploeger and Birner 2016). Moreover, it can help to identify and interpret model biases that are obscured in integrated measures such as the age of air and thus can help improve the long-term predictions of tracer distributions (Ray et al. 2016). In the present work, we use the TEM tracer continuity equation to investigate transport of e90 in the UTLS, including terms that are usually negligible in the stratosphere but can be important in the troposphere, such as transport by convection and vertical diffusion due to turbulent processes in the boundary layer. In the usual global climate model grids (~1°–2° longitude and latitude) these processes are not resolved but are parameterized, and thus the details can potentially be strongly model dependent (e.g., Orbe et al. 2017). Nevertheless, it is important to include them as they play an important role in tropospheric tracer transport (Hess 2005; Erukhimova and Bowman 2006; Orbe et al. 2017).

A fundamental open question is how an evolving climate may impact global tracer distributions. Understanding future changes in tracer transport is key not only for assessing trends in the radiative properties of the atmosphere but also for air quality issues. Robust responses of the large-scale circulation to climate change in models include a lifting of the tropopause and a strengthening of the upper flank of the subtropical jets, while a slight poleward shift in the near-surface westerlies and a widening of the Hadley cell are more uncertain and model-dependent changes (Lorenz and DeWeaver 2007; Vallis et al. 2015). In the stratosphere, there is a consensus among models that age of air will decrease in the future due to an acceleration of the residual circulation (e.g., Butchart 2014).

While long-term trends in middle atmosphere transport circulation have been a subject of active research in the last decades, only a few model studies have addressed future tracer transport trends at lower levels. Rind et al. (2001) examined global changes in several long-lived tracers [including chlorofluorocarbons (CFCs) and SF_6] in a doubled-CO_2 world, and obtained 30% stronger troposphere-to-stratosphere exchange in the tropics, which was attributed to enhanced stratospheric upwelling and tropical deep convection. They also noted a reduction in lower-tropospheric concentrations, which was attributed to increased convective transport. In contrast, Held and Soden (2006) demonstrated that a reduction of convective transport out of the boundary layer is an expected robust response to climate change, linked to the higher water vapor concentrations in the lower troposphere. Holzer and Boer (2001) imposed pulse surface emissions of artificial tracers over four different locations and used the Green function approach to derive the climatology of transport under present and future conditions. Their results suggested an overall weakening of transport in the troposphere in the future, leading to longer transit time scales. Using a two-box model, they estimated a 25% reduction in the tropospheric tracer burden and an equivalent increase in

the stratosphere by the end of the twenty-first century, attributed mainly to a small rise in the tropopause. Fang et al. (2011) examined future changes in a CO-like artificial tracer, and their results also highlighted an important role of the tropopause changes in determining future trends in tracer distribution. Using a dry dynamical core, Orbe et al. (2013) analyzed the changes in tropospheric transport for separate air masses originating in the stratosphere and near the surface. Their results suggested a decrease in stratosphere-to-troposphere transport at high latitudes due to reduced residual circulation downwelling at the tropopause, along with enhanced isentropic eddy mixing across the subtropical tropopause. They also found enhanced transport out of the midlatitude boundary layer toward the polar free troposphere in the future. In contrast with other works, this idealized model study did not produce increased future concentrations of tropospheric tracers in the stratosphere.

In the present work, we examine UTLS tracer transport and the long-term trends over the period 1955–2099 using simulations with the Whole Atmosphere Community Climate Model (WACCM). The model and the specific simulations used are introduced in section 2. Section 3 presents the climatological distribution of e90 and the contribution of the different transport terms. Section 4 focuses on the interannual variability of e90, and section 5 examines the e90 trends and their dynamical origin. Section 6 presents the main conclusions and a discussion of the results in light of previous works.

2. Model simulations

We use runs of the Whole Atmosphere Community Climate Model. WACCM is the atmospheric component of the Community Earth System Model, version 1 (CESM1), which extends to altitudes up to near 140 km. These runs use version 4 of WACCM, based on CAM4 (Neale et al. 2013). It has 66 vertical levels, the horizontal resolution is 2.5° longitude × 1.9° latitude, and the vertical resolution is 1.2–1.5 km in the UTLS. The chemistry module is an update to Kinnison et al. (2007) for use in the Chemistry–Climate Model Initiative (CCMI; Eyring et al. 2013; Morgenstern et al. 2017) and includes ~180 species and more than 470 chemical reactions. The transport scheme is a finite-volume dynamical core, which has a Lagrangian coordinate in the vertical (Lin 2004; Lauritzen et al. 2011). Neale et al. (2013) describe the improvements in CAM4 with respect to its predecessor, including the impacts of new convective parameterizations and the finite-volume dynamical core. Marsh et al. (2013) provide further information of the version of the model used here. The orographic and nonorographic gravity wave parameterizations are described in Garcia et al. (2007) and Richter et al. (2010), respectively, with recent modifications described in Garcia et al. (2017).

The runs used here are the REF-C2 reference runs carried out for CCMI, which have coupled atmosphere, ocean, ice, and land components of the CESM (Morgenstern et al. 2017). These runs cover the period 1955–2099, they have fully interactive atmospheric chemistry, and the emissions follow the representative concentration pathway 6.0 (RCP6.0) scenario. Although three members are available for the CESM WACCM REF-C2 runs, all the results shown here are very similar for each member, and thus we only include results for the first member. These WACCM runs have an imposed quasi-biennial oscillation (QBO), with equatorial stratospheric winds between 86 and 4 hPa relaxed toward observed variability, repeated in the future (Marsh et al. 2013).

The e90 tracer is emitted homogeneously at the surface (over both land and ocean), with a constant flux of 2.7736×10^{11} mol cm^{-2} s^{-1}.

3. Climatological structure of e90

a. Annual mean

Figure 1 shows the latitude–altitude cross section of annual-mean e90 averaged over the entire REF-C2 period (1955–2099). The concentration of e90 is maximum near the surface, is relatively homogeneous in the free troposphere (changing only from around 150 ppbv near the surface to 90 ppbv at the tropopause), and has sharp gradients across and just above the tropopause (decreasing to 10 ppbv just 5 km above the tropopause). The large gradients in the UTLS are due to the 90 day lifetime of the tracer, which is slow relative to the vertical transport in the troposphere but fast compared to the rate of vertical transport in the stratosphere. This makes the distribution of e90 particularly sensitive to circulation changes near the tropopause. The e90 contour of 90 ppbv, used by Prather et al. (2011) to define the chemical tropopause, coincides roughly with the lapse-rate tropopause, although it is slightly lower, especially in the extratropics (and more so in the SH). Near the surface, e90 has a nonuniform latitudinal structure despite the uniform emissions, with high surface concentrations extending to higher levels near the equator and at high latitudes, reflecting different rates of ventilation out of the boundary layer, as will be shown below. Within the relatively well-mixed tropospheric distribution, two tongues of depleted e90 concentrations can be observed in the subtropical middle and upper

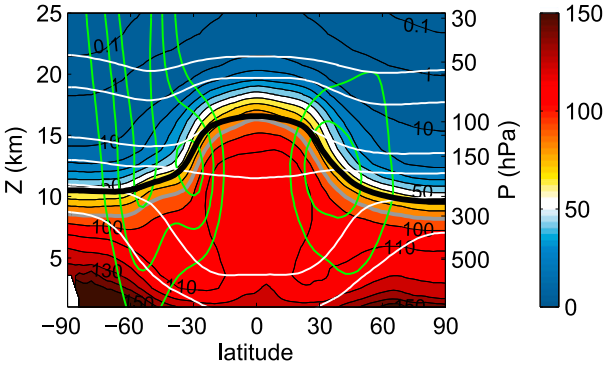

FIG. 1. Climatology of e90 concentrations (shading; ppbv) for the annual mean in the REF-C2 WACCM run as a function of latitude and log-pressure altitude $Z = -H\ln(p/p_0)$ with $H = 7$ km and $p_0 = 1000$ hPa. The 90-ppbv contour is shown in gray. The thick black contour shows the lapse-rate tropopause. The green contours show the zonal-mean wind (10 m s^{-1} spacing; zero omitted), and the white contours show selected isentropes (300, 320, 350, 380, 450, and 500 K).

troposphere, approximately extending along the 320-K isentrope in each hemisphere (see the 110-ppbv contour). Randel et al. (2016) hypothesized that these structures could be linked to isentropic transport of air from the extratropical lower stratosphere. The contribution of the different transport mechanisms in shaping this structure will be analyzed below using the TEM framework. The overall e90 structure in Fig. 1 is consistent with that of other artificial tracers in previous studies mentioned in the introduction (e.g., Bowman and Carrie 2002; Hall and Plumb 1994), but e90 highlights the transport processes in the region around the tropopause.

To interpret the mean structure of e90 in Fig. 1, we compute the terms in the TEM continuity equation for e90. This equation can be written for the zonal-mean tracer mixing ratio $\overline{\chi}$ on pressure levels as (Andrews et al. 1987)

$$\overline{\chi}_t = -\overline{v}^*\overline{\chi}_y - \overline{w}^*\overline{\chi}_z + \nabla\cdot\mathbf{M} + \overline{L} + \overline{X}, \qquad (1)$$

where $\mathbf{M} = -e^{-z/H}[\overline{v'\chi'} - (\overline{v'T'}/S)\overline{\chi}_z, \overline{w'\chi'} + (\overline{v'T'}/S)\overline{\chi}_y]$ is the eddy tracer flux vector. The subscripts indicate partial derivatives; $(\overline{v}^*, \overline{w}^*)$ are the residual circulation components; overbars indicate zonal mean and primes deviations from it; $S = HN^2/R$, where N^2 is the Brunt–Väisälä frequency squared, the scale height is taken as $H = 7$ km, and R is the ideal gas constant; and the log-pressure altitude is $z = H\ln(p_0/p)$, with $p_0 = 1000$ hPa. The term $\overline{L}$ represents e90 loss and can be expressed as $\overline{L} = -\tau^{-1}\overline{\chi}$, with $\tau = 90$ days. The term $\overline{X}$ on the right-hand side of Eq. (1) accounts for subgrid processes that are not resolved in the model, including transport by the shallow and deep convection schemes and by vertical diffusion due to parameterized boundary layer mixing. Transport due to breaking nonorographic gravity waves (not shown) is very small in the UTLS. On the other hand, transport by breaking orographic gravity waves is not an available output in this version of the model, and thus it is not included. However, as will be discussed later, this is likely a small term in the UTLS.

Figure 2 shows the different terms in the annual-mean TEM balance as a function of latitude and pressure. The calculations are done using daily mean output, and the results are averaged over 6 years at the beginning of the simulation (1956–61). The e90 tendency, on the left-hand side of Eq. (1), equals zero for the annual average and thus it is not included in Fig. 2. Advection by the residual circulation increases e90 concentrations in the tropical UTLS and decreases them in the extratropics, particularly strongly over high latitudes in the troposphere (Fig. 2a). The eddy transport term $\nabla\cdot\mathbf{M}$, a function of eddy tracer fluxes, can be approximately associated with the tracer transport resulting from two-way mixing of air masses, although this term does not strictly isolate the irreversible process of mixing (e.g., Nakamura 1996). The direction of the eddy flux vector $\mathbf{M}$ (denoted by arrows in Fig. 2b) is mainly along isentropes everywhere except in the tropical troposphere, where the vertical component of the flux dominates (Fig. 2b). Isentropic transport above the subtropical jets leads to decreases in tropical/subtropical e90 and increases poleward of the jet cores. In the troposphere, isentropic eddy transport leads to exchange of air between the lower-troposphere middle latitudes and the UTLS high latitudes. This two-directional isentropic mixing on the upper and lower flanks of the jets is closely related with breaking of medium-scale (wavenumbers ~4–7) transient Rossby waves (Abalos et al. 2016b). Vertical eddy mixing in the UT increases e90 concentrations everywhere between 30°N and 30°S and between about 320 and 380 K, making an important contribution to the balance in that region, which has not been highlighted before to our knowledge. Interestingly, this vertical eddy transport overshoots the tropopause at the equator, increasing e90 concentrations in the deep tropics of the lowermost stratosphere.

Figure 2c shows annual-mean e90 transport by the convective parameterizations in WACCM (shallow and deep convection). The convective influence, which increases e90 values in the free troposphere, reaches highest altitudes in the tropics [around 12 km, consistent with the typical altitude of deep convective towers (e.g., Johnson et al. 1999)]. However, the region of strongest convective outflow in the deep tropics is located at a lower level (near 5 km). Note the relative minima in

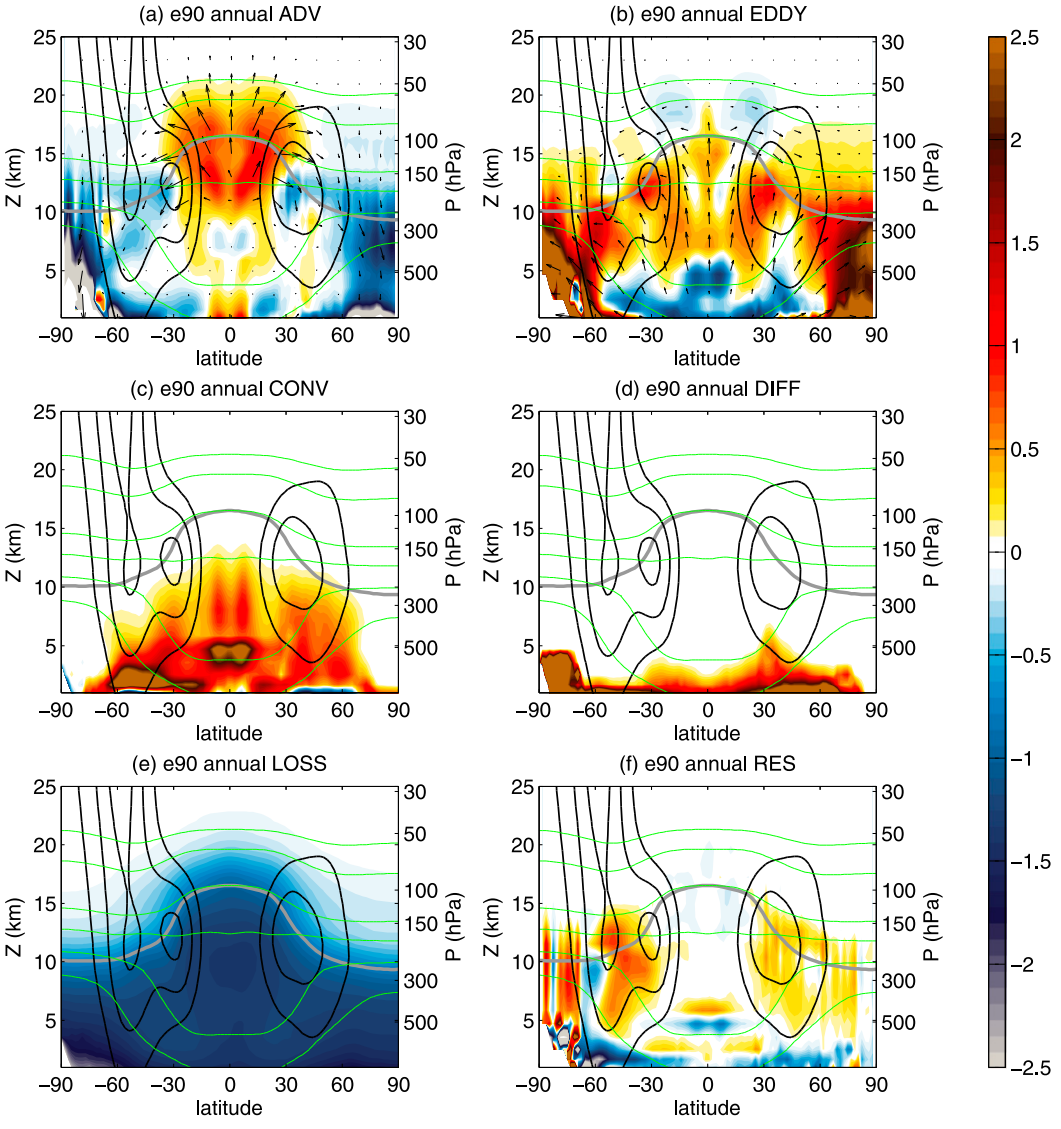

FIG. 2. Terms in the e90 TEM balance (ppbv day^{-1}): (a) advection by the residual circulation, (b) eddy transport, (c) shallow and deep convection, (d) vertical diffusion, (e) chemical loss, and (f) the balance residual. Results are shown for the annual mean over 1956–61 of the REF-C2 run. The vectors in (a) depict the residual circulation advective fluxes and in (b) the eddy tracer flux vector **M** [see Eq. (1)]. The vectors are scaled to account for the difference in the vertical vs horizontal dimensions and divided by a function of density to enhance the upper levels. The gray contour shows the lapse-rate tropopause. The black contours show the zonal-mean wind (10 m s^{-1} spacing; zero omitted), and the green contours show selected isentropes (300, 320, 350, 380, 450, and 500 K).

convective transport above 5 km in the subtropics of both hemispheres, consistent with suppressed convection in these regions of climatological subsidence by the Hadley cell. Figure 2d shows the e90 tendency due to (explicit) vertical diffusion in the model. This term is largest in the lower troposphere, related to e90 transport in the boundary layer. The specified 90-day chemical loss tendency is shown in Fig. 2e, and it shows the expected structure proportional to the e90 climatology in Fig. 1. Finally, Fig. 2f shows the residual of the balance, expressed as the additional term needed on the right-hand side of Eq. (1) to make the annual-mean tracer tendency equal zero. This residual is in general smaller than the other terms, but it is nonnegligible in some regions, especially in the SH extratropics.

There are several factors that contribute to the nonzero residual. First, the transport scheme has an implicit numerical diffusion, both in the vertical and in the horizontal, which is not included in the TEM balance. This diffusion is larger in regions of small-scale features

associated with strong gradients. Second, as mentioned in section 2, this version of WACCM uses a vertically Lagrangian finite-volume transport scheme, in which the vertical coordinate is initialized as the terrain-following hybrid coordinate and then is allowed to evolve freely as a material surface (Lin 2004). In this scheme, vertical transport is computed by remapping the tracer into model levels. Hence, the vertical velocity used to compute the TEM balance is a diagnostic variable, not used to advect the tracer in the model. In addition, the TEM calculations are carried out using daily mean data, while in the model the advection time step is much smaller (less than 10 min in these simulations). Because the average of the product is not equal to the product of the averages, this leads to differences in the products in Eq. (1). Finally, the TEM calculations in Fig. 2 are carried out on pressure levels (or equivalently on log-pressure altitude), while in the model transport is performed on hybrid levels, which are terrain following below ~100 hPa. The linear interpolation to pressure levels introduces numerical errors that might contribute to prevent exact closing of the balance. All these numerical issues contribute to a nonzero residual in the balance, although their relative importance cannot be assessed from our analyses.

The numerical origin of the residual is confirmed by the fact that the balance can be closed when the transport tendency is computed directly inside the model's dynamical core. The total tracer-resolved transport computed by the model is shown in Fig. 3a, as compared to the resolved transport computed from Eq. (1) (i.e., the sum of the advective and the eddy transport terms, shown in Fig. 3b). The total transport terms are overall very similar, and the difference between Figs. 3a and 3b almost exactly equals the residual in Fig. 2e (not shown). This implies that the imbalance is due to differences in the numerical methods employed inside the model's transport scheme and those using the model output described above, and not due to other processes not included in the balance (such as nonorographic gravity waves). Note that the main differences (i.e., the larger balance residuals) in the UTLS are found near the jets, especially in the SH. We have checked that the residual obtained from computing the zonal-mean transport from three-dimensional (3D) advection from the model output is almost equal to the residual in the TEM balance in Fig. 2e (not shown). Examining the residual of the 3D balance, we have found that large residuals generally have the form of filamentary structures along strong westerly winds, especially in the SH UTLS. Hence, the larger residuals are found in regions of strong wind shear around the jets and near the tropopause, characterized by frequent wave breaking and associated formation of

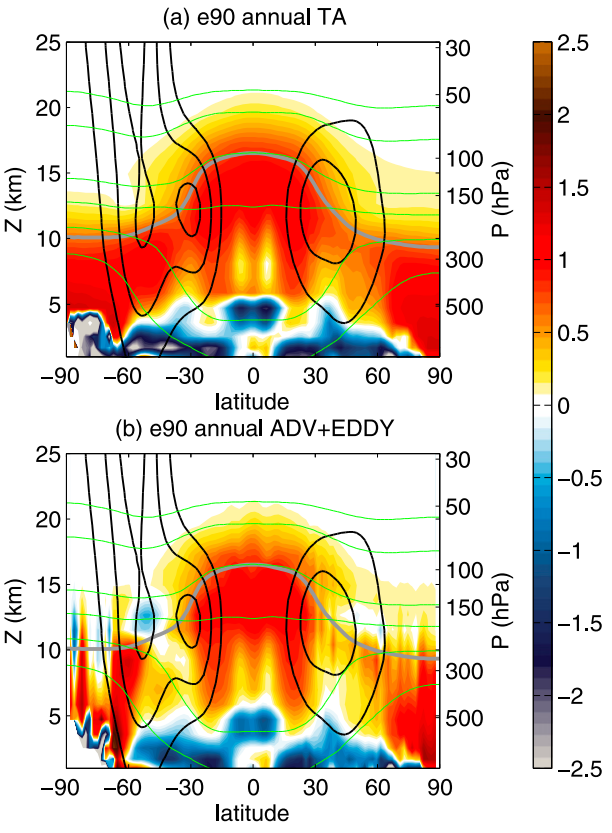

FIG. 3. Comparison of annual-mean e90 resolved transport computed (a) directly inside the transport scheme of the model and (b) from the TEM calculations (advection plus eddy). Results are shown for the annual mean over 1956–61 of the REF-C2 run. The gray contour shows the lapse-rate tropopause. The black contours show the zonal-mean wind (10 m s^{-1} spacing; zero omitted), and the green contours show selected isentropes (300, 320, 350, 380, 450, and 500 K).

fine filaments in the tracers. These small-scale structures are smoothed out by numerical diffusion in the model transport scheme (and in the atmosphere eventually by molecular mixing), but this implicit diffusion is not included in the TEM balance. The small-scale structures also enhance the differences between the instantaneous and daily mean calculations. In addition, there are particularly large values of the residual over regions with high orography (particularly over the Himalayas, the Rocky Mountains and the Andes). In these regions there are large variations in vertical motion over small horizontal scales, leading to small-scale features and sharp gradients over small regions that enhance the numerical differences, contributing to the residual in the zonal-mean balance. In summary, there are non-negligible residuals in the SH extratropical UTLS which have a numerical origin (Fig. 2f), and in the rest of the paper we take special care when examining the balance terms in this region. Specifically, the contribution of the

different terms in the TEM budget [Eq. (1)] to the e90 seasonality and to the long-term trends will be questioned in this region of largest uncertainties.

From the TEM analysis in Fig. 2 the layers with relatively low e90 below the subtropical jets in the zonal-mean climatological structure of e90 (Fig. 1) cannot be attributed to a single transport mechanism, but rather result from a combination of them. Overall, relatively small transport tendencies lead to relatively e90-depleted air in these regions. A fundamental aspect is the suppressed convective transport in the subtropics, which does not replenish these regions with young air of high near-surface e90 concentrations. In addition, there are near-zero advective tendencies in the subtropical troposphere, where the residual circulation slowly overturns connecting the subtropical downwelling of the Hadley cell with the polar downwelling. This slow zonal-mean transport results in relative aged air in the subtropical and midlatitude troposphere. Finally, isentropic mixing with high-latitude and lower-stratospheric air also plays a role, mostly in middle latitudes (30–60°N/S) between about 500–300 hPa. The zonal-mean climatological tongue-like shapes arise only when all these terms are combined.

b. Seasonal cycle

Figure 4 shows the e90 seasonal cycle on selected isentropes above, across, and below the subtropical jets (380, 350, and 320 K; see Fig. 1 for the location of these isentropes). At all levels there is a seasonal displacement of the concentrations toward the summer hemisphere, and there is a hemispheric asymmetry, with farther poleward extension in the boreal than in the austral hemisphere. This is related to an asymmetry in the strength of the summer jets, with the boreal summer jet weaker and located farther poleward, due to the presence of the large-scale monsoon circulations. At high latitudes, e90 is more depleted in the winter hemisphere at all levels. Note that there is a strong seasonality in the height of the isentropes at high latitudes, with isentropes around 2 km higher in winter than in summer (see Fig. 5). This is clearly seen in the seasonal shift in the location of the tropopause at 320 K, which in the NH moves from the subtropics in winter to high latitudes in summer. Near the tropical tropopause (380 K), there is a seasonal cycle in tropical e90, with higher values in boreal winter. The meridional gradients separating tropical from extratropical values are stronger in the winter subtropics, consistent with the subtropical jets acting as transport barriers. These winter gradients are strongest at 350 K, as this isentrope cuts through the core of the subtropical jets. Note that the e90 tropopause in winter coincides with

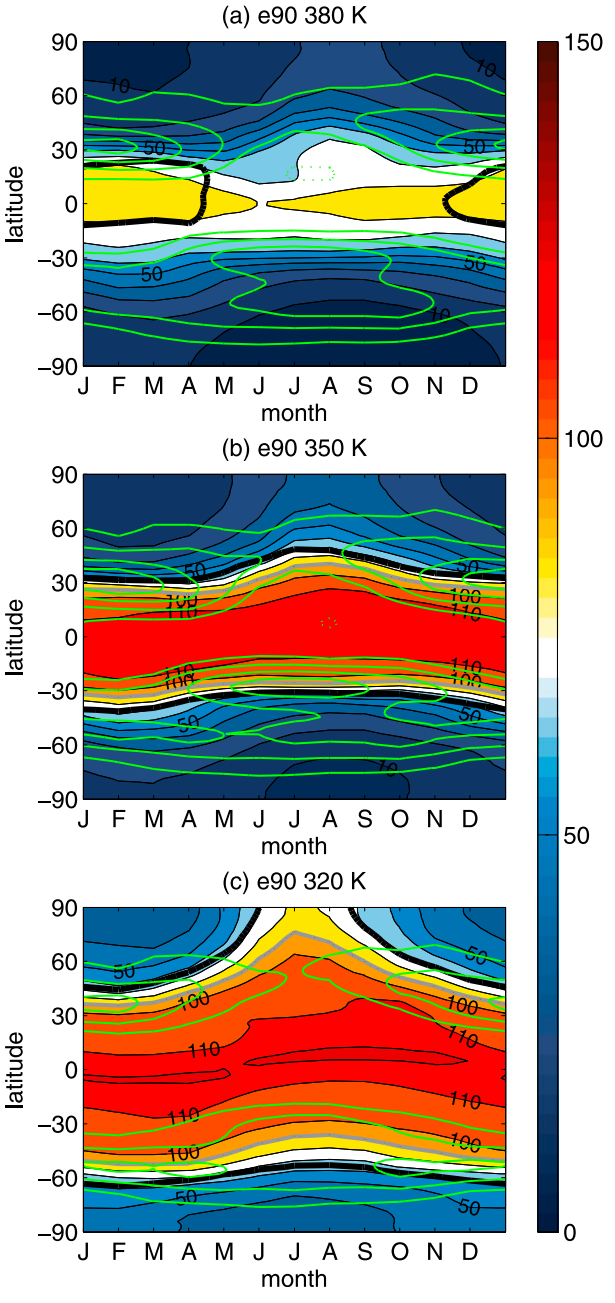

FIG. 4. Seasonality of e90 concentrations (shading; ppbv) on different isentropic levels (380, 350, and 320 K) in the REF-C2 WACCM run as a function of latitude. The 90-ppbv contour is shown in gray, and the thermal tropopause is shown by the thick black line. The green contours show the zonal-mean wind (10 m s^{-1} spacing; zero omitted).

the core of the jets, corresponding with the region of strongest gradients. Also at 320 K the e90 tropopause is located in the region of stronger winds on the lower flanks of the jets. The subtropical tongues of relatively low e90 observed in Fig. 1 are seen on this isentrope as regions of relatively homogeneous e90 concentrations

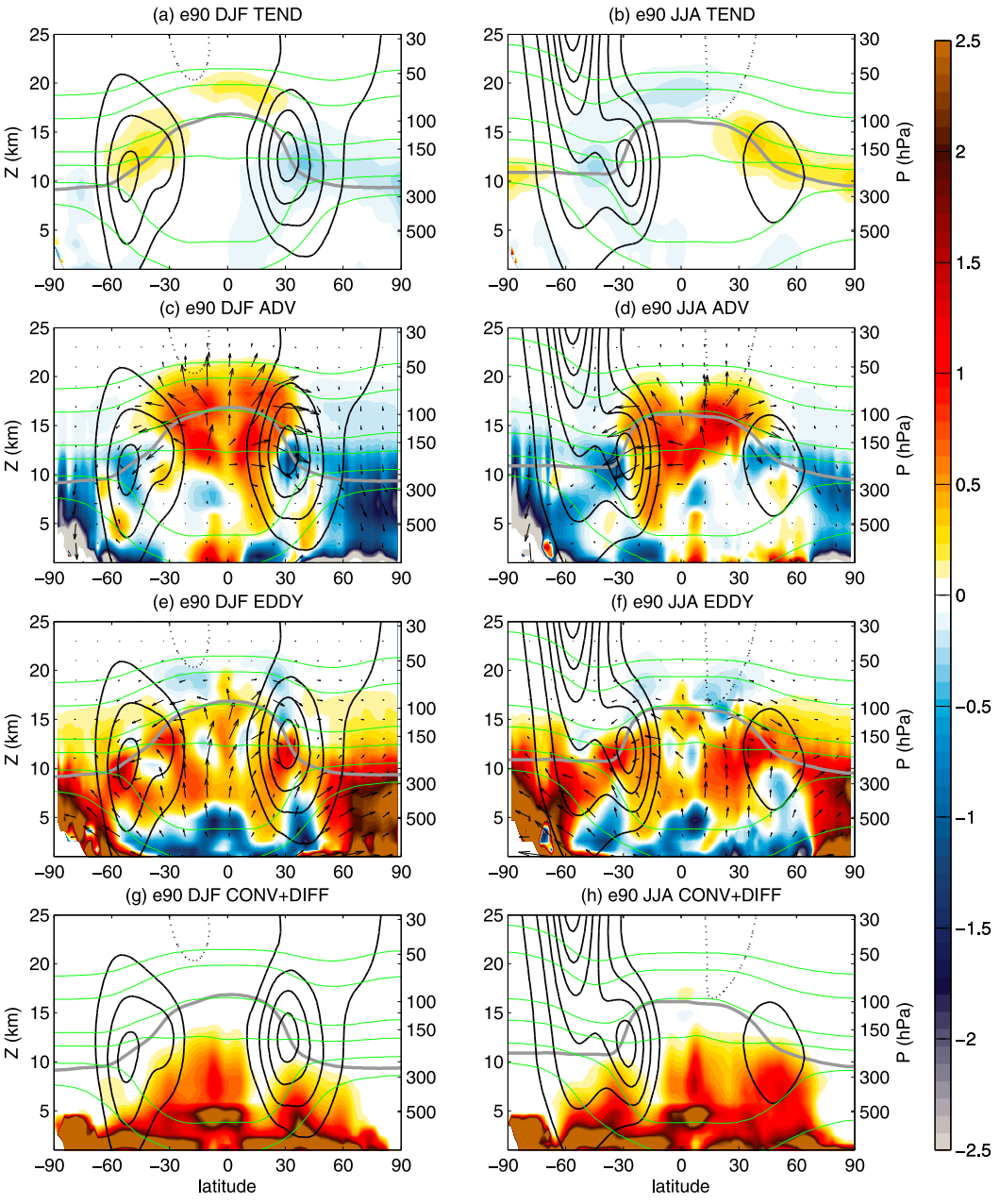

FIG. 5. Terms in the e90 TEM balance (ppbv day^{-1}) for (left) DJF and (right) JJA. (a),(b) Tendencies, (c),(d) advection by the mean residual circulation, (e),(f) eddy transport, and (g),(h) subgrid transport (deep and shallow convection plus boundary layer diffusion). Results are shown for the seasonal mean over 1956–61 of the REF-C2 run. The vectors in (c) and (d) depict the residual circulation advective fluxes and in (e) and (f) the eddy tracer flux vector **M** [see Eq. (1)]. The vectors are scaled to account for the difference in the vertical vs horizontal dimensions and divided by a function of density to enhance the upper levels. The gray contour shows the lapse-rate tropopause. The black contours show the zonal-mean wind (10 m s^{-1} spacing; zero omitted), and the green contours show selected isentropes (300, 320, 350, 380, 450, and 500 K).

over a large portion of the subtropics, which move poleward during the summer following the tropopause. Finally, there is a maximum near the equator at this lower level, slightly displaced into the summer hemisphere.

To examine the contribution of the different transport terms to the seasonality in UTLS e90, Fig. 5 shows the e90 tendency and resolved transport terms for the seasons December–February (DJF) and June–August (JJA). The tracer tendency (Figs. 5a,b) shows positive

values in the tropical lower stratosphere in DJF and negative in JJA, consistent with the e90 seasonality at 380 K in Fig. 4a. This seasonality in the tropical lower stratosphere is linked to transport by the Brewer–Dobson circulation (BDC) upwelling, which is stronger in DJF (see Figs. 5c,d). In JJA the weaker e90 positive tendency by upwelling is smaller than the e90 loss, resulting in a negative net tendency (the loss term is not shown in Fig. 5). Near the core of the subtropical jets, there are net tendencies of opposite sign in each hemisphere (Figs. 5a,b), consistent with the behavior in Fig. 4b. This is linked to stronger downwelling in the shallow branch of the BDC in the winter hemisphere, leading to negative e90 tendencies in this season (Figs. 5c,d). At high latitudes the sign of the e90 tendency is the same as in the subtropics in the NH, while in the SH it changes sign (Figs. 5a,b). The seasonality in the NH high latitudes is driven by e90 decrease in DJF due to stronger BDC downwelling (Fig. 5c) and increase by isentropic mixing in JJA (Fig. 5f). In contrast, in the SH polar UTLS the downwelling in JJA is not enough to overcome the effect of strong isentropic mixing from the troposphere (Fig. 5f). However, as mentioned above, the attribution to the different transport terms is subject to larger uncertainty in this region (poleward of ~45°S) because of the nonnegligible residual (see Fig. 2f).

In the extratropical troposphere there is no significant seasonality in e90 because the stronger downwelling at high latitudes in winter (Figs. 5c,d) is compensated by the stronger eddy transport in this season (Figs. 5e,f). The stronger isentropic eddy two-way mixing in winter (and spring, not shown) in the extratropical troposphere is consistent with more frequent synoptic and mesoscale baroclinic wave disturbances in this season. Specifically, warm conveyor belts in frontal circulation systems are associated with efficient mixing between the boundary layer and the free troposphere [Stohl et al. (2003) and references therein]. In the tropical troposphere the seasonality of the Hadley cell is clearly visible, with ascent displaced toward the summer hemisphere following the intertropical convergence zone (ITCZ) and cross-hemispheric transport toward the winter hemisphere. Note that the downwelling branch of the Hadley cell does not decrease but rather increases e90 concentrations near 20°N/S (except below ~5 km). This is due to the reversed (positive) sign of the vertical e90 gradients in these regions, associated with the upper flank of the tonguelike structures in both hemispheres highlighted in Fig. 1. Vertical eddy mixing in the tropical UT increases e90 concentrations between ~5 and 10 km (or approximately between 320 and 380 K) and decreases them below in both seasons, and is slightly larger in the summer hemisphere (especially in JJA). The lower-tropospheric e90 is replenished by convective transport out of the boundary layer, as shown in Figs. 5g and 5h. The small e90 negative tendencies in the tropical/subtropical troposphere (Figs. 5a,b) are linked to the pronounced minima in convective transport in the winter subtropics, which coincide with the region of subsidence of the Hadley cell (Figs. 5g,h). Figures 5g and 5h also show that e90 transport by tropical deep convection peaks on the summer side of the equator (stronger in JJA), such that the double peak in convective transport around the equator in Fig. 2e is an effect of the annual averaging. This shift of convection with the ITCZ is reflected in the seasonal displacement of the near-equatorial e90 maximum at 320 K in Fig. 4c.

Figure 5 suggests that the contribution of the different terms to the maintenance of the low-e90 layers in the subtropical troposphere varies with the season. Specifically, in the winter hemisphere suppressed convection at low latitudes and enhanced isentropic eddy transport in midlatitudes are most relevant, while in the summer hemisphere near-zero advective transport is the main contributor to the depleted e90. On the other hand, the old-air tongues are thinner in the winter hemisphere (not shown), because they are confined by the Hadley cell downwelling on their equatorward and upper flank (Figs. 5c,d) and by isentropic eddy transport in their poleward and lower flank (Figs. 5e,f).

4. Interannual variability

Figure 6a shows the main mode of interannual variability in e90, computed by obtaining the first empirical orthogonal function (EOF; e.g., von Storch and Zwiers 2002) of the annual-mean detrended e90 field over the period 1955–2099. We note that if the field is not detrended the main mode is the linear trend, which will be examined in the next section. The pattern in Fig. 6a shows enhanced e90 in the tropical lower stratosphere and reduced e90 concentrations in the subtropical lowermost stratosphere, extending to high latitudes above the tropopause. In addition, the subtropical patterns extend deep into the subtropical troposphere. Figure 6b shows the regression of the first principal component (PC1) of e90 (i.e., the time series associated with the EOF in Fig. 6a) onto the detrended residual circulation streamfunction. Note that positive Ψ^* anomalies indicate clockwise circulation and vice versa. The streamfunction structure shows an enhanced shallow branch of the residual circulation with tropical lower-stratospheric upwelling and subtropical downwelling in both hemispheres. This lower-stratospheric circulation is connected to an enhanced narrow tropical

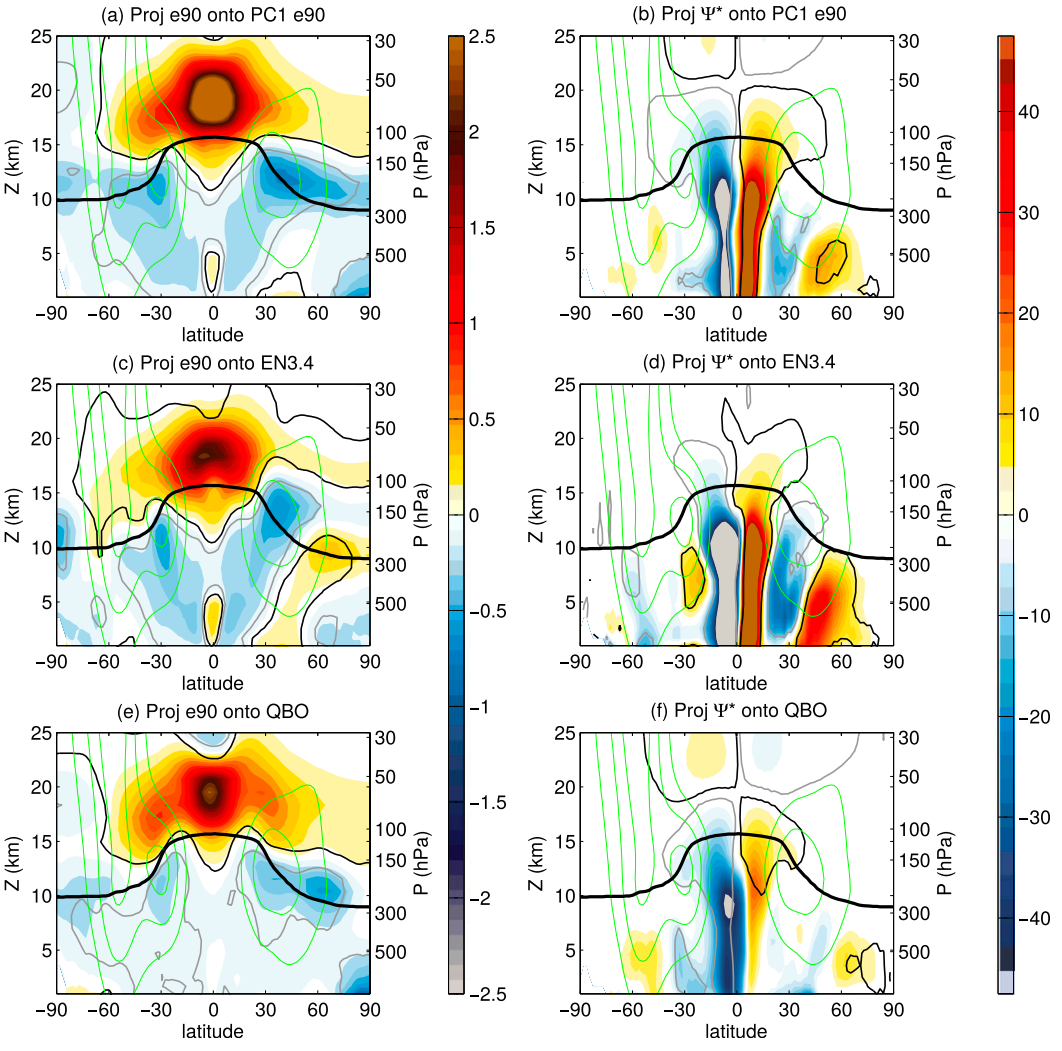

FIG. 6. Regressions (units are per standard deviation of the index) of (left) e90 (ppbv) and (right) the residual circulation streamfunction (kg m^{-1} s^{-1}) onto the (a),(b) first principal component of e90 (based on detrended annual-mean fields), (c),(d) annual mean El Niño-3.4 index, and (e),(f) annual mean QBO index. The contours show the regions where the correlations are statistically significant at the 99% level based on the Student's *t* test (black: positive; gray: negative). The black thick contour shows the lapse-rate tropopause, and the green contours show the zonal-mean wind (10 m s^{-1} spacing; zero omitted).

tropospheric circulation (i.e., a narrowing and vertical extension of the top of the Hadley cell). Above the shallow branch there are two cells of opposite sense in each hemisphere. The structure of the residual circulation in Fig. 6b is consistent with the patterns in the e90 regression in Fig. 6a, given the strong e90 background gradients across the tropopause. The enhanced upwelling leads to the positive e90 values in the tropical lower stratosphere, and the downwelling leads to the reduced e90 near the core of the subtropical jets. The negative e90 patterns extending into the troposphere are consistent with enhanced stratosphere-to-troposphere transport in the subtropics implied by the residual streamfunction.

Figures 6c and 6d show the regressions of e90 and the residual streamfunction (after detrending the fields) onto ENSO, using El Niño 3.4 index (N3.4; Trenberth 1997) computed from the same REF-C2 run (note that surface air temperature was used in the N3.4 region instead of sea surface temperature, because of data availability). The resulting patterns are similar to those of the e90 first EOF, indicating that the main mode of interannual variability in e90 is closely related to ENSO. The linear correlation between N3.4 and e90 PC1 is 0.55. The impact of ENSO on tracer distribution in the UTLS has been examined in previous works, in particular focusing on ozone (e.g., Randel et al. 2009; Calvo et al. 2010; Oman et al. 2013).

These works show a similar pattern in lower-stratospheric ozone as that in Fig. 6c (with opposite sign), due to enhanced transport by the stratospheric residual circulation. In addition, Oman et al. (2013) extended the observed ozone response into the UT by combining satellite data from two instruments and found an extension of the subtropical anomalies into the tropical troposphere, similar to that in Fig. 6c, over the Pacific Ocean. That work also showed that this behavior was captured in a chemistry–climate model simulation. Given that ozone has chemical sources and sinks, different in the troposphere and the stratosphere, the ozone patterns could potentially result from a combination of changes in dynamical and chemical processes [as seen for the long-term trends in tropical upper-tropospheric ozone (e.g., Banerjee et al. 2016)]. In contrast, the e90 pattern in Fig. 6c isolates the ENSO impact on UTLS tracer transport unambiguously.

This enhanced stratosphere-to-troposphere transport associated with ENSO is further examined using tracer–tracer correlations of e90 with the artificial tracer ST80, which is a standard CCMI tracer specifically designed to evaluate stratosphere-to-troposphere exchange in the models (Eyring et al. 2013). By definition, ST80 is held constant in the stratosphere above 80 hPa and decays with a lifetime of 25 days below that level. The ST80 climatology of the tracer has fixed concentrations above 80 hPa, very strong gradients across the tropopause, and small values in the troposphere, because of the short lifetime (not shown). Figures 7a and 7b show the tracer–tracer correlation plot for the annual-mean tracer concentrations in the subtropical upper troposphere in each hemisphere, where e90 is depleted by enhanced transport from the stratosphere during warm ENSO events (see Fig. 6c). Specifically, the tracers are averaged over 20°–30°N/S and 500–200 hPa. There is a clear separation between positive and negative ENSO events (defined as years when N3.4 exceeds one standard deviation), with high values of ST80 and low values of e90 associated with El Niño events, and vice versa for La Niña events. Because ST80 originates in the stratosphere and e90 in the troposphere, this high, negative correlation confirms that warm ENSO events enhance transport from the stratosphere into the subtropical troposphere.

Figures 6e and 6f show the regressions of detrended e90 and the residual streamfunction onto the quasi-biennial oscillation, using the first EOF of the equatorial zonal wind in the 70–10-hPa layer following Wallace et al. (1993). The correlation between e90 PC1 and the QBO index is 0.56. The regression patterns in Fig. 6f show a quadrupole very similar to that seen in Fig. 6b, with opposite-sense Ψ^* cells above and below 20 km. The e90 regressions demonstrate that the QBO accounts

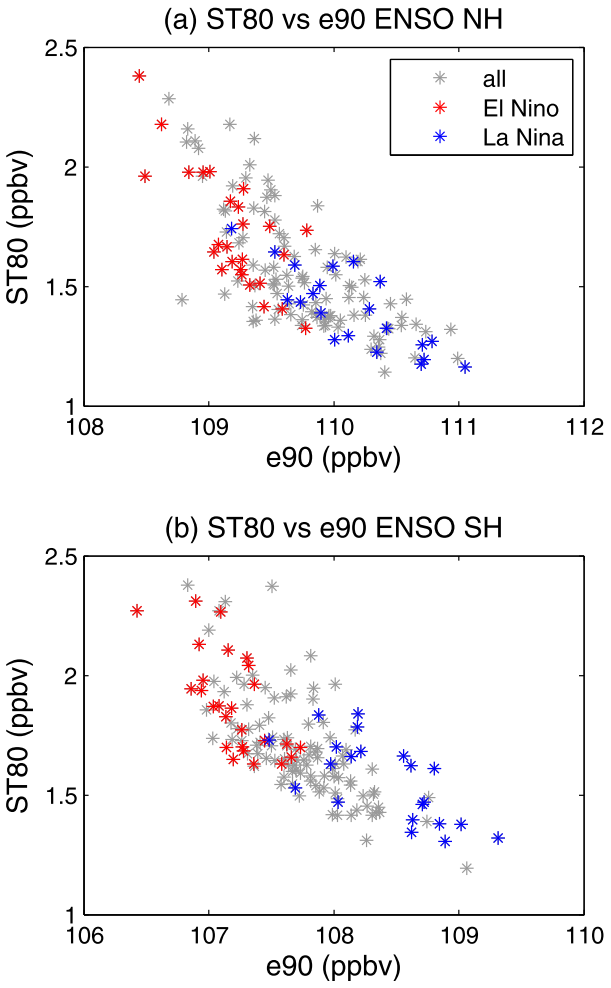

FIG. 7. Tracer–tracer correlation plot (ppbv) of annual-average ST80 vs e90 over 1955–2099, with warm and cold ENSO events indicated. The points correspond to the concentrations averaged over 500–200 hPa and 20°–30° latitude in the (a) NH and (b) SH.

for the stratospheric features of the e90 EOF1 pattern (Fig. 6a) that are not in the ENSO regression (Fig. 6c), in particular the extension of e90 positive anomalies from the tropics into the extratropical lower stratosphere. In contrast with ENSO, the QBO regression patterns do not extend into the tropical troposphere. We note that the QBO is forced in these runs by nudging to repeating observed equatorial winds, and such an unvarying QBO is inconsistent with a changing climate [although there is currently no consensus on how the QBO will respond to climate change, it is reasonable to expect adjustments to the changing dynamics (e.g., Kawatani and Hamilton 2013)]. Nevertheless, the imposed QBO winds induce changes in the residual circulation and thus impact the interannual variabiliy of tracer concentrations in the tropical stratosphere. The important role of ENSO and the QBO on e90 variability can be summarized by the

fact that together they explain 70% of the variance in the first mode of interannual variability in e90 (of which ENSO alone explains 30%). The relative importance of ENSO and the QBO in driving interannual variability in the UTLS is likely dependent on the specific tracer gradients (e.g., a shorter-lived tracer than e90 may have less influence on a stratospheric process such as the QBO). The fact that the first EOF of e90 includes common variance both with ENSO (internally generated by the model) and the QBO (externally imposed) implies that the EOF statistical technique does not separate the effects on e90 of these two dynamical modes of variability.

5. Trends 1955–2099

a. Annual-mean trends

Figure 8a shows the annual-mean trends in e90 calculated over 1955–2099, which feature increased concentrations in the tropical lower stratosphere and in a layer just above the extratropical tropopause. In the troposphere there are relatively homogeneous negative e90 trends in both hemispheres, slightly stronger in the lower-troposphere midlatitudes. The linear trends over the 145 years are largely statistically significant, and thus we do not show contours of statistical significance in this plot and in the following. Note that the relative trends (not shown) increase with height across the tropopause because of the decreasing mean concentrations (see Fig. 1), such that the trends in the troposphere are around 0.1% decade^{-1}, while those in the lower stratosphere are around 2% decade^{-1}. The trend patterns in Fig. 8a suggest a connection with the tropopause. To explore this, Fig. 8b shows the e90 trends relative to the tropopause height. These are obtained by remapping the monthly e90 field onto tropopause-relative coordinates (i.e., levels are defined by the distance to the tropopause) and then computing the trends. For an easier comparison with Fig. 8a, the tropopause-relative trends have been remapped back onto pressure levels using the climatological average of the tropopause log-pressure altitude. Figure 8b shows positive trends in the tropical lower stratosphere, weaker than those in Fig. 8a, and near-zero trends (or even negative) above the extratropical tropopause. In the troposphere, the negative trends are enhanced in the tropopause-relative case, mostly at middle and high latitudes. On the other hand, the e90 trends in the tropical middle and upper troposphere are reduced. The differences between the two panels of Fig. 8 highlight that a large fraction of the trends in e90 are strongly coupled to the trends in the tropopause height. The tropopause altitude has a linear

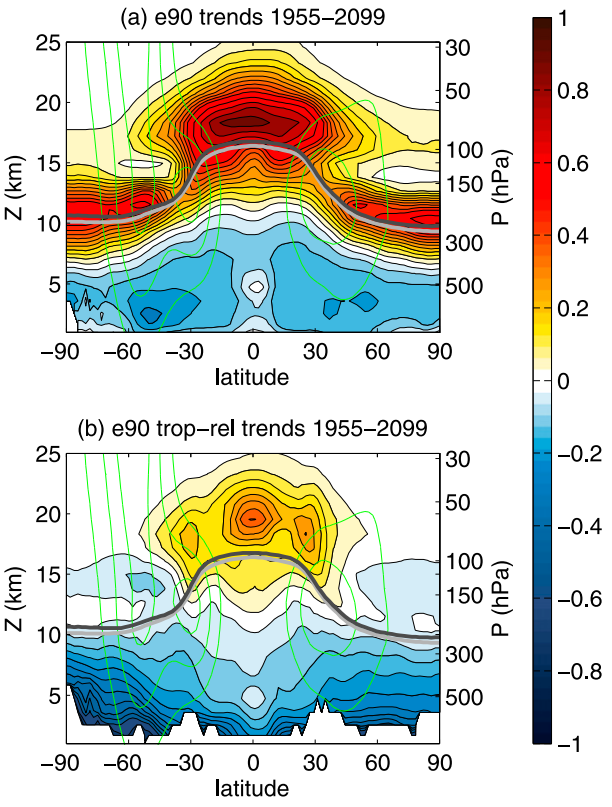

FIG. 8. Annual-mean trends in e90 (ppbv decade^{-1}) using (a) log-pressure altitude and (b) tropopause-relative log-pressure altitude as the vertical coordinate. The gray lines indicate the altitude of the tropopause for the past (light gray) and the future (dark gray), using the first and last 10 years of the simulation, respectively. Note that the tropopause-relative trends have been remapped onto pressure coordinates using the climatological mean tropopause altitude.

trend of about 30 m decade^{-1} in this run, a value consistent with other models (e.g., Vallis et al. 2015), such that over the period of the simulations it rises approximately 430 m globally, which is ~1/3 of the vertical grid spacing of the model (the past and future tropopauses are shown in Fig. 8). The fact that such a small change in the location of the tropopause is associated with a large difference in the tracer trends between the two coordinate systems highlights the key role of this chemical and dynamical boundary.

Oberländer-Hayn et al. (2016) recently noted that the long-term trends in the stratospheric residual circulation are also substantially modified (reduced) when considering the changes in the tropopause in three CCMI models (not including WACCM). Figure 9 shows the trends in the residual mass streamfunction over the region of interest in our WACCM run, both in pressure and tropopause-relative coordinates. The trends in Fig. 9a show the expected acceleration of the BDC in the

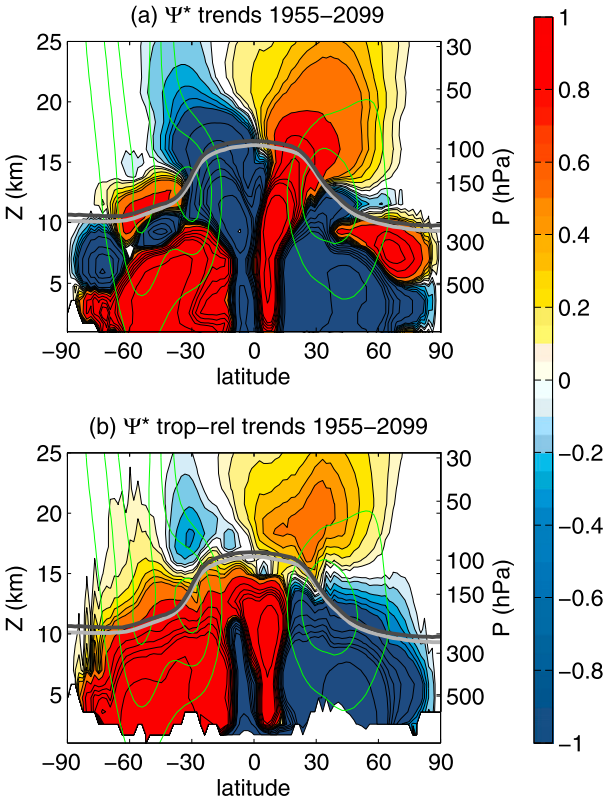

FIG. 9. As in Fig. 8, but for annual-mean trends in Ψ* (kg m^{-1} s^{-1} decade^{-1}).

stratosphere. In agreement with Oberländer-Hayn et al. (2016), Fig. 9b shows that the stratospheric residual circulation trends are reduced when considering the displacement of the tropopause. Note that, while the rise in the tropopause and the strengthening BDC both act to increase e90 in the tropical lower stratosphere, they have opposite effects on the extratropical lower-stratospheric e90 concentrations. In the tropical troposphere, Fig. 9a shows a narrowing and strengthening of the upper part of the circulation [consistent with Oberländer-Hayn et al. (2016)]. The tropical/subtropical UTLS residual circulation trends are similar to the circulation response to ENSO (Fig. 6d), suggesting that the tropical/subtropical tropospheric concentrations of stratospheric tracers may be enhanced in the future, because of enhanced stratosphere-to-troposphere advective transport. A tracer–tracer correlation plot of e90 versus ST80 in these regions (not shown) shows a similar separation between past and future years as that between La Niña and El Niño years in Fig. 7, supporting this hypothesis. Note that these changes are closely linked to the height of the tropical tropopause, as the pattern changes in Fig. 9b. The seasonal trends show acceleration of the upper part of the Hadley cell and deceleration of the lower part in DJF and JJA (not shown), consistent with the results of Rind et al. (2001). In the extratropical troposphere the overturning circulation is predicted to decelerate in both hemispheres, except near the extratropical tropopause (Fig. 9a). On the other hand, the tropopause-relative trends show hemispheric-scale decreasing circulation patterns, which overshoot the extratropical tropopause (Fig. 9b).

To further examine future dynamical changes in the UTLS, Fig. 10a shows the trends in the Eliassen–Palm (EP) flux and its divergence (e.g., Andrews et al. 1987). There is enhanced EP flux convergence in the subtropical lower stratosphere in both hemispheres, consistent with the dynamical mechanism for strengthening of the BDC shallow branch proposed in previous works (Garcia and Randel 2008; Shepherd and McLandress 2011). This mechanism implies enhanced upward and equatorward propagation of Rossby waves (as seen in the EP flux trends) due to the changes in critical lines associated with stronger winds in the upper flanks of the subtropical jets, highlighted in Fig. 10a. In the extratropical UTLS of both hemispheres there are dipoles in the EP flux divergence trends, with convergence near the tropopause and divergence below, implying an upward shift of the region of main convergence. This structure suggests a coupling with the rise in the tropopause, and indeed the dipoles disappear for the tropopause-relative trends, as shown in Fig. 10c. The EP flux trends in the lower stratosphere are significantly reduced in tropopause-relative coordinates, consistent with weaker BDC acceleration in Fig. 9b. In the troposphere, the positive trends in midlatitudes are consistent with the hemispheric deceleration of residual circulation cells in Fig. 9b. The small trends in the tropopause altitude are associated with substantial changes in the thermodynamic UTLS structure. In particular, there is an overall reduction in static stability across and above the tropopause both in the tropics and extratropics, shown in Fig. 10b, linked to the stratospheric cooling and tropospheric warming. The strong coupling between the tropopause rise and the trends in static stability near the tropopause is demonstrated by the fact that the trends disappear in tropopause-based coordinates (Fig. 10d). The reduced stability around the extratropical tropopause can lead to changes in the propagation and dissipation of the waves in this region (Matsuno 1970). In turn, these changes in the location of wave breaking (Fig. 10a) drive changes in tracer transport near the tropopause by modifying both the residual circulation and isentropic mixing. In the next

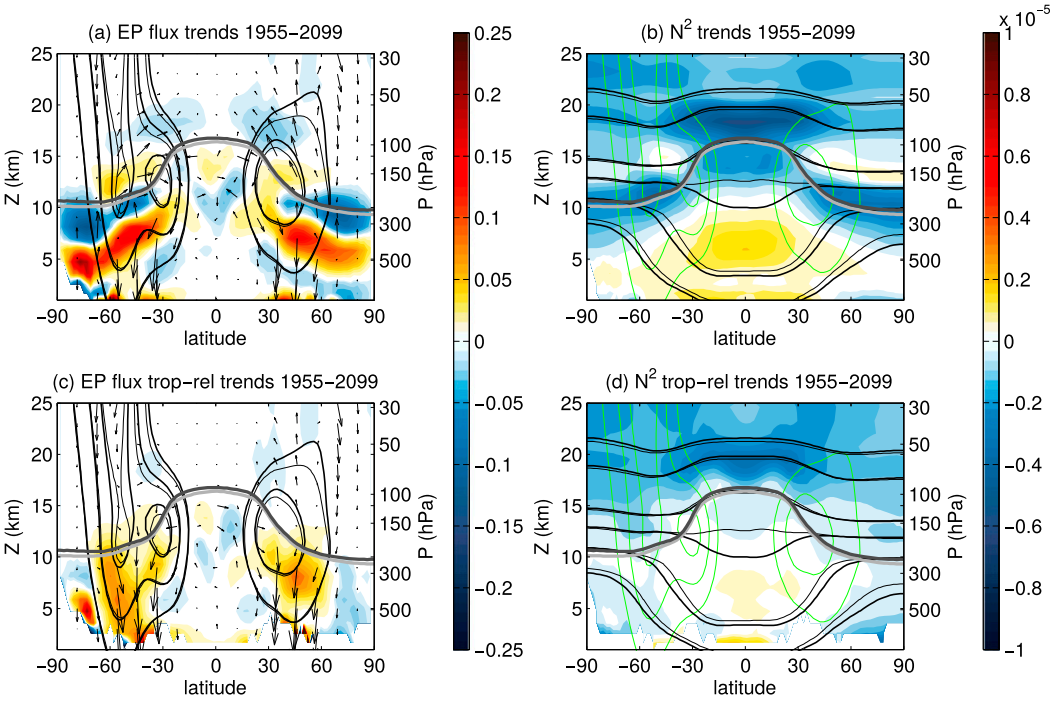

FIG. 10. (left) Annual-mean trends in EP flux (vectors) and mass-weighted EP flux divergence [shading; $\mathrm{DF} = \nabla \cdot \mathbf{F} e^{z/H}/(a\cos\phi)$; $\mathrm{m\,s^{-1}\,day^{-1}\,decade^{-1}}$] using (a) log-pressure and (c) tropopause-relative coordinates. The black contours in (a) and (c) show the zonal wind climatology for the past (thin, 1956–61 average) and the future (thick, 2091–96 average), with $10\,\mathrm{m\,s^{-1}}$ spacing and zero omitted. (right) Annual-mean trends in Brunt–Väisälä frequency squared N^2 ($\mathrm{s^{-2}\,decade^{-1}}$) using (b) log-pressure and (d) tropopause-relative coordinates. The black contours in (b) and (d) show the potential temperature climatology (levels: 300, 320, 350, 380, 450, and 500 K) for the past (thin, 1956–61 average) and the future (thick, 2091–96 average). The gray lines indicate the altitude of the tropopause for the past (light gray) and the future (dark gray), using the first and last 10 years of the simulation, respectively. Note that the tropopause-relative trends have been remapped onto pressure coordinates using the climatological mean tropopause altitude.

subsection we examine the trends in the different transport terms for e90.

b. *Changes in transport terms*

To attribute the contribution from each transport term to the net change in e90 concentration from past to the future, Eq. (1) can be written as

$$\overline{\chi} = \tau(-\overline{v}^*\overline{\chi}_y - \overline{w}^*\overline{\chi}_z + \nabla \cdot \mathbf{M} + \overline{X}), \qquad (2)$$

where we have taken into account that $\overline{\chi}_t = 0$ when averaged over the annual mean, and we have expressed the loss term as $\overline{L} = -\overline{\chi}/\tau$. Equation (2) allows direct attribution of the change in e90 concentration $\overline{\chi}_{\mathrm{future}} - \overline{\chi}_{\mathrm{past}}$ to changes in the different terms. Figure 11a shows this difference using 6 years at the beginning (1956–61) and at the end (2091–96) of the simulation to represent the past and future. The fact that the difference (Fig. 11a) is very similar to the trend pattern in Fig. 8a indicates that the differences between these two groups of 6 years on the extremes of the run are representative the long-term linear trends. The contribution of the resolved transport (computed inside the model transport scheme) to the net e90 change is shown in Fig. 11b, and the contribution of the changes in subgrid-scale processes is shown in Fig. 11c. The e90 trends above the tropopause are entirely associated with changes in resolved transport. In the troposphere there is a near cancellation between the trends in resolved and subgrid transport, with a net small negative tendency. In the tropical middle to upper troposphere, e90 concentrations increase because of enhanced deep convective transport, but this is compensated by a decrease due to the resolved transport, such that the net trends in this region are near zero and slightly negative (Fig. 11a). The negative e90 trends in the extratropical middle and upper troposphere are linked to resolved transport, partly compensated by enhanced deep convection. On the other hand, there is reduced e90 transport by convection in the lower troposphere (below 5 km), which is larger than the increase due to resolved transport. This

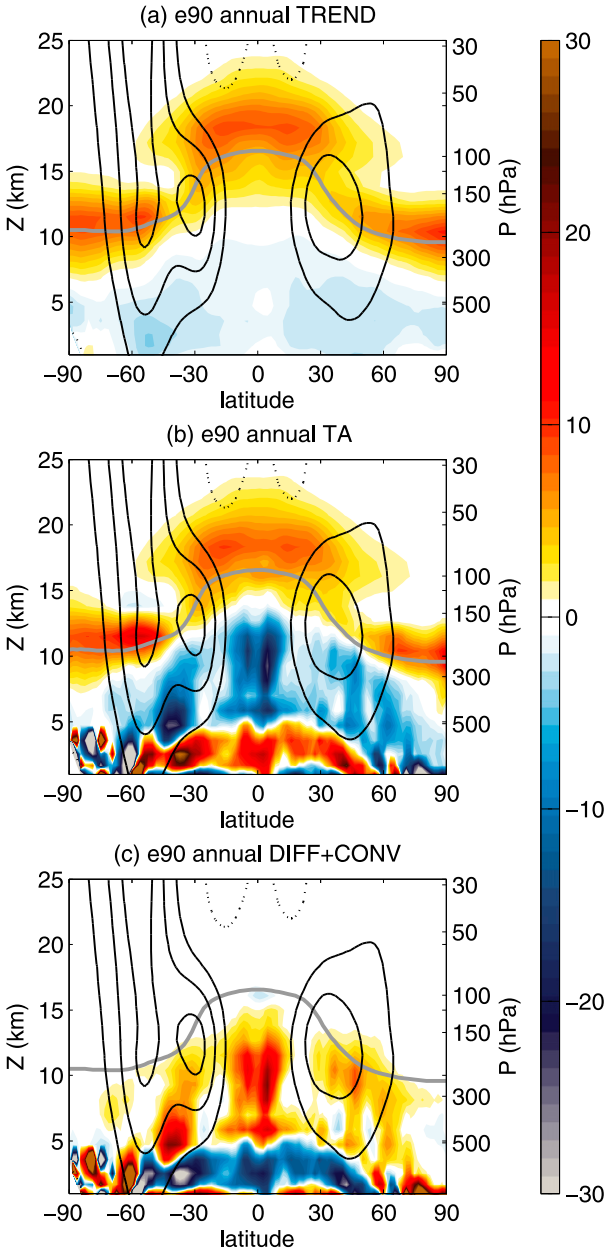

FIG. 11. Difference (ppbv) of future (2091–96) minus past (1956–61) of the terms in the tracer equation of e90 [Eq. (2)]. (a) Tracer concentration, (b) resolved transport, and (c) subgrid transport (deep and shallow convection plus boundary layer diffusion).

decrease in convective transport out of the boundary layer is consistent with reduced convective mass flux (integrated over the atmospheric column) in a future climate (Held and Soden 2006). In addition, Fig. 11c shows that deep convective transport reaching higher levels (above ~5 km) in the model will be strengthened in the future. A similar pattern of decrease in the lower troposphere and increase above is found in the trends of convective mass flux in these model runs (not shown).

The trends in the resolved transport can be further decomposed into trends in the advective and eddy components (Fig. 12). We note again that there is little confidence in assessing the contribution from the different transport terms in the SH high latitudes where the residual of the TEM balance is not negligible (see Fig. 2f), and thus here we avoid analyzing this region. Figure 12a confirms that the e90 increase in the tropical lower stratosphere is linked to the increase in the tropical upwelling, and thus to stronger vertical troposphere-to-stratosphere transport in the future. Correspondingly, the reduced tropopause-relative e90 trends in this region are due to the weaker vertical advection in these coordinates (consistent with Fig. 9). The advective term also shows negative e90 trends associated with increased downwelling over the extratropical lower stratosphere (Fig. 12a). This decrease is compensated by the positive trend in the eddy term at high latitudes (Fig. 12b), such that the total transport trend is positive, as seen in Fig. 11b. Hence, the high-latitude positive trends in e90 in this region (Fig. 8a) can be attributed to an increase in eddy mixing above the extratropical tropopause. This result is clearer for the NH where the balance residual is smaller. This enhanced mixing near the tropopause (Fig. 12b) is strongly coupled to the vertical shift in Rossby wave breaking (Fig. 10a), which in turn is associated with the rise of the tropopause (Fig. 10b). Consistently, the trends in eddy transport near the extratropical tropopause disappear in tropopause-relative coordinates (not shown). On the other hand, isentropic transport is substantially reduced in the extratropical troposphere, which accounts for the negative trend in net resolved transport in this region (Fig. 11b). The fact that the resolved and subgrid transports mirror each other in Fig. 11 suggests that the weaker resolved (eddy) transport is a response to the reduced convective tracer transport out of the boundary layer into the free troposphere, which weakens the tracer gradients along the isentropes. The net negative e90 trend in extratropical troposphere (Fig. 11a) is weaker than that in the eddy term (Fig. 12b) because of the partial cancellation by positive trends in the advective term (Fig. 12a). Note that this partial cancellation does not occur in tropopause-relative coordinates because of the changes in the residual circulation near the extratropical tropopause (Fig. 9b), and this results in stronger negative e90 trends (Fig. 8b). Finally, the positive trends in the tropical lower troposphere in Fig. 11b are linked to

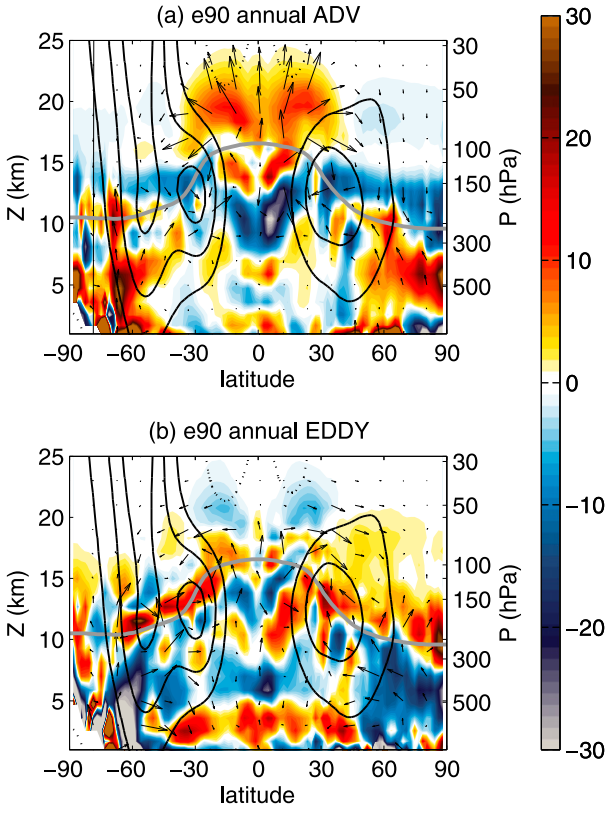

FIG. 12. Difference (ppbv) of future (2091–96) minus past (1956–61) of the terms in the TEM tracer equation of e90 [Eq. (2)]. (a) Advective transport and (b) eddy transport. The arrows show the changes for future minus past in the residual circulation advective flux in (a) and the eddy flux vector in (b).

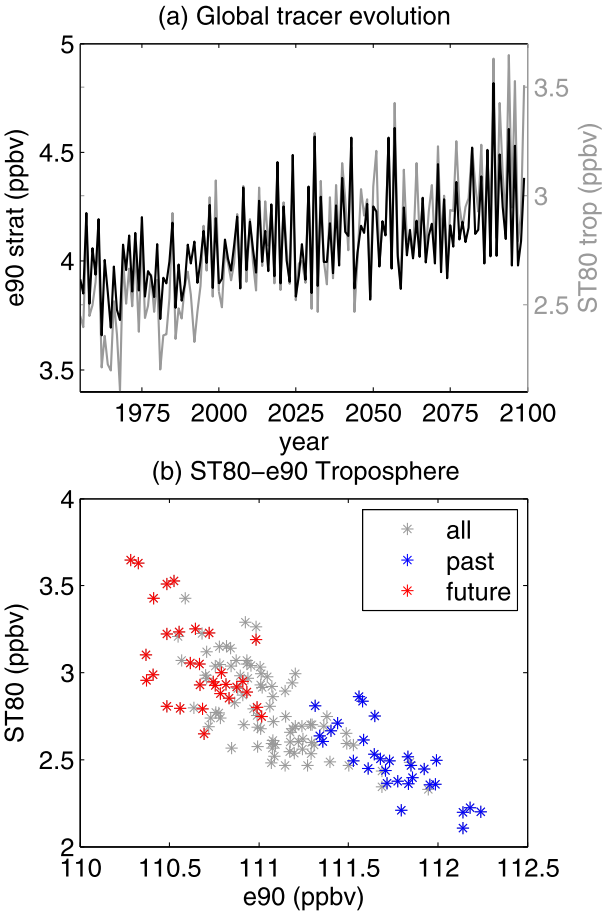

FIG. 13. (a) Time series of e90 concentration averaged over the stratosphere and ST80 averaged over the troposphere (ppbv). (b) Tracer–tracer correlation plot of annual-average ST80 vs e90 over 1955–2099 averaged globally in the troposphere (ppbv), with the 30 first and last years of the simulation highlighted.

weakened vertical mixing between the lower and middle troposphere (Fig. 12b), possibly responding to smaller near-surface concentrations. However, these are overcompensated by the reduced convective transport (Fig. 11c), leading to a net reduction of e90 in the tropical lower to middle troposphere. In summary, the main drivers of the observed long-term trends in e90 are as follows:

- Increase in the tropical lower stratosphere due to stronger advection by upwelling.
- Increase in the lowermost extratropical stratosphere due to stronger eddy mixing.
- Decrease in the extratropical troposphere due to weaker isentropic eddy mixing.
- Decrease in the lower troposphere due to weaker convective transport.

A relevant question concerning the trends in UTLS transport is whether the rate of tracer exchange between the troposphere and the stratosphere will change in a future climate. To examine the trends in the net troposphere-to-stratosphere transport, Fig. 13a shows time series of annual-mean e90 concentrations averaged for the entire stratosphere (computed using the tropopause-relative vertical coodinate, to account for changes in tropopause height). The net increase in stratospheric e90 (linear trend of 0.58% decade^{-1}, statistically significant at the 95% level) implies an increase in troposphere-to-stratosphere transport. Figure 13a also shows the time series of annual-mean tropospheric-mean ST80 concentrations, which show a statistically significant linear trend of 1.74% decade^{-1}. Note that both time series have significant common interannual variability (linear correlation of 0.92), which indicates a strong covariance of stratosphere–troposphere transport in both directions. Figure 13b shows the scatterplot of ST80 versus e90 concentrations (as in Fig. 7), averaged over the entire troposphere.

The coherent decrease in e90 and increase in ST80 further suggests a strengthening net stratosphere-to-troposphere transport with climate change.

6. Conclusions and discussion

The artificial tracer e90 is used to study UTLS tracer transport in WACCM. This tracer is emitted homogeneously at the surface and has a lifetime of 90 days in the atmosphere, which results in particularly strong gradients across the tropopause because of the different transport time scales in the troposphere and the stratosphere (Fig. 1). We analyze the transport terms leading to the climatological zonal-mean structure of e90 using the TEM tracer continuity equation [Eq. (1)]. Resolved transport in the troposphere is influenced by subgrid-scale (parameterized) convective transport out of the boundary layer, as the latter determines to a large extent the tracer concentrations and gradients in the free troposphere. Overall, our results highlight a clear distinction in the UTLS between the tropics, dominated by vertical motion, and the extratropics, dominated by isentropic mixing (Fig. 2). This picture is in agreement with previous works, which consider the troposphere as divided in three main regions (the extratropics of each hemisphere and the tropics), with rapid tracer dispersion in each region but slow exchange between them (e.g., Erukhimova and Bowman 2006). Note that our analyses focus on levels up to 25 km, and thus mostly below the stratospheric polar night jets and subtropical transport barriers, features that fundamentally influence transport at higher levels in the stratosphere (e.g., Plumb 2002).

In the tropical UTLS, deep convective transport, vertical eddy transport associated with two-way mixing, and advection by the Hadley cell and the Brewer–Dobson circulation efficiently transport e90 from the surface into the stratosphere. Interestingly, vertical eddy mixing plays a significant role in the tropical e90 balance, acting as a connection between the convective uplift in the lower troposphere (below ~5–10 km) and the advective transport by the Hadley cell in the upper troposphere (above ~12 km). This term is mostly determined by the vertical eddy tracer flux $\overline{w'\chi'}$. Seasonal-mean maps of the eddy products $w'\chi'$ at 500 hPa show that these are closely related to the zonal anomalies in the vertical wind over regions of enhanced deep convection in the tropics and along the storm tracks on the east coast of the continents (not shown). Although in principle the vertical wind is subject to large uncertainties due to the specific characteristics of the transport scheme in WACCM, the balance is relatively well closed in the region where this flux is important, suggesting that there are not large numerical issues in this vertical eddy mixing term.

Isentropic eddy transport in the extratropical troposphere is stronger in the winter hemisphere (Figs. 5e,f), consistent with stronger storm-track activity and eddy kinetic energy in this season. Isentropic transport above the subtropical jets also peaks in winter and spring in the NH above 100 hPa, except over the layer 150–100 hPa (approximately along 380 K), where it is maximum in summer. A similar change with altitude in the seasonality of isentropic eddy transport in the NH was observed in Abalos et al. (2013) for ozone. The maximum in JJA near 380 K is linked to the presence of the Asian summer monsoon, which is associated with significant mixing between low and high latitudes in the lower stratosphere (e.g., Hegglin and Shepherd 2007; Ploeger et al. 2013). At higher levels the influence of the Asian monsoon is reduced and the isentropic transport peaks in late winter and spring (Abalos et al. 2013). Isentropic mixing in the SH above the jet peaks in summer (DJF), when the upper flank of the jet is weak enough to allow eddy transport.

The tongues of relatively low e90 mixing ratio in the troposphere around the 320-K isentrope (approximately at 30°–60°N/S, 500–300 hPa; see Fig. 1) result from a combination of factors, including suppressed deep convection in the winter subtropics, near-zero advective transport in the summer subtropics and middle latitudes and isentropic mixing with high-latitude and extratropical lower-stratospheric air. The first two mechanisms imply that these regions are relatively quiescent, and thus e90 is depleted without being efficiently replenished. This is consistent with the conclusions of Prather et al. (2011) regarding the nonstratospheric origin of the oldest air in the troposphere (as measured by the smallest e90 concentrations). An alternative hypothesis that has been proposed is that these layers are mainly associated with isentropic mixing with high-latitude UTLS air (Randel et al. 2016). Previous works have shown large effective diffusivity values in the baroclinic region below the subtropical jets (e.g., Haynes and Shuckburgh 2000; Abalos et al. 2016a). These works considered adiabatic two-dimensional transport, but the tropical lower troposphere is dominated by vertical motion (Chen and Plumb 2014; see also Figs. 2 and 5).

Our TEM analyses (which include 3D transport) do highlight an important role of isentropic eddy mixing leading to the exchange of tracers between high and low latitudes, including across the extratropical tropopause (Figs. 2b, 5e,f). However, the depletion of e90 due to this eddy transport peaks in the lower-troposphere middle latitudes (negative tendencies around 30°–60°N/S, below 500 hPa), a region where e90 is efficiently replenished by

convection. Hence, although isentropic mixing likely contributes to maintain these e90-depleted tongues in the middle latitudes above the region of strongest convective influence (i.e., above 500 hPa), it is surely not the only mechanism. The limited temporal and spatial resolution of our analyses could underestimate isentropic eddy transport, which is ultimately linked to filamentary structures that are not fully resolved. Nevertheless, previous works show a good agreement between the climatological structure of effective diffusivity and that of eddy diffusivity, a proxy of isentropic mixing estimated from the isentropic eddy tracer flux (see Abalos et al. 2016b). Finally, we note that the climatology of tracers with stratospheric sources (such as ST80, not shown) does not present equivalent tonguelike structures (with enhanced ST80 concentrations) as those seen in e90. We have checked that this is not an effect of the different lifetimes of the tracers. This further supports the conclusion that isentropic mixing with high-latitude UTLS air alone is not sufficient to explain these climatological structures.

Interannual variability shows an important role of ENSO throughout the UTLS and the QBO in the lower stratosphere (Fig. 6). In agreement with previous works, positive ENSO events enhance the shallow branch of the Brewer–Dobson circulation (e.g., Randel et al. 2009; Calvo et al. 2010). In the lower stratosphere, warm ENSO events are associated with enhanced e90 in the tropics and reduced e90 in the subtropics and middle latitudes. The negative anomalies in the subtropical lower stratosphere extend deep into the troposphere following the residual circulation anomalies, which lead to enhanced stratosphere-to-troposphere advective transport in the subtropics during El Niño years. This is confirmed by examining the tracer–tracer correlation plots of e90 versus a purely stratospheric tracer, ST80 (Fig. 7). This result is in agreement with the enhancement of ozone over the Pacific region during El Niño events pointed out by Oman et al. (2013).

The long-term trends in e90 (1955–2099) show an increase above the tropopause and a decrease in the troposphere (Fig. 8a). These UTLS trends are linked to a rise in tropopause altitude to a large extent (Fig. 8b), consistent with the recent work on the BDC trends by Oberländer-Hayn et al. (2016). The stratospheric e90 trends are attributed to enhanced residual circulation in the tropics and to changes in eddy transport in the extratropics (Fig. 12), both associated with changes in the wave propagation and dissipation due to changes in the jets and static stability (Fig. 10). While the extratropical trends disappear in tropopause-relative coordinates, the trends in tropical lower-stratospheric e90 remain slightly positive (Fig. 9b). This is not seen in the results of Fang et al. (2011), which show near-zero trends everywhere in tropopause-relative coordinates. The similarity of the tropopause-relative trends in residual circulation (Fig. 9b) to those of other CCMI models in Oberländer-Hayn et al. (2016) suggests that this is a robust result. This result is different from that of Orbe et al. (2013), which shows zero trend in upwelling at the tropopause and reduced downwelling at high latitudes. The difference could be due to the very different models (dry dynamical core versus fully coupled climate model), and also to the fact that stratospheric tracers in Orbe et al. (2013) have fixed concentrations in the stratosphere, which make them insensitive to changes in stratospheric circulation.

The overall e90 reduction of the troposphere is in agreement with previous works mentioned in the introduction (e.g., Holzer and Boer 2001). Our results show that in WACCM this is linked to 1) weakening of isentropic eddy transport in the extratropical troposphere, 2) enhanced removal by advective transport into the stratosphere in the tropical upper troposphere, and 3) reduced convective transport in the lower troposphere (Figs. 11, 12). Note that the reduced isentropic eddy exchange in the extratropical troposphere is opposite to the increase of air transported out of the midlatitude boundary layer toward the pole found by Orbe et al. (2013). In that work, future changes in tropospheric transport are mainly a response to the poleward shift of the jets and associated changes in eddy kinetic energy. Although the simulations analyzed here show a similar poleward shift in baroclinicity (not shown), our results suggest an overall weakening of the tropospheric extratropical circulation. This difference could arise from the absence of convection in the dry dynamical core. Indeed, our WACCM results suggest an important role of changes in convective transport out of the boundary layer, which affects the resolved transport through modifications of the tracer gradients. An indication of this influence is the mirror images of the trends in the resolved and subgrid-scale transports (Figs. 11b,c).

The e90 decrease in the tropical troposphere (between approximately 5 and 12 km) is similar to the pattern of negative trends in the CO-like tracer in Fang et al. (2011). While in that work the negative trends were attributed to reduced convective mass flux, our TEM analysis demonstrates that they are due to changes in advective transport in WACCM, in particular an upward extension of the top of the Hadley cell. Our model simulations show a reduction in total convective mass flux (integrated in the column), in agreement with Held and Soden (2006). However, the trends in spatially resolved convective mass flux, very similar to the trends in

e90 convective transport in Fig. 11c, show that this reduction is limited to the lower troposphere (below ~5 km), with a (weaker) increase in deep convection above ~5 km. The robustness of these results involving changes in parameterized processes such as convection across comprehensive chemistry–climate models is an interesting topic to be explored in future works. Finally, using tropopause-relative coordinates, we show a net increase of e90 in the stratosphere and a net increase of ST80 in the troposphere, which suggest an enhancement of stratosphere–troposphere exchange in both directions of about 1% decade^{-1} with climate change (Fig. 13).

Acknowledgments. We are thankful to Mengchu Tao and Peter Lauritzen for useful discussions and to Peter Hitchcock and Charles Bardeen for insightful comments on the manuscript. We thank the editor, as well as Shigeo Yoden, and an anonymous reviewer for a constructive review of the paper. Marta Abalos was funded by the NASA ACMAP Program and by the Research Grant Atracción de Talento Comunidad de Madrid (reference 2016–T2/AMB–1405). NCAR is sponsored by the National Science Foundation. We acknowledge excellent computing and storage resources provided by NCAR's Computational and Information Systems Laboratory (CISL).

REFERENCES

Abalos, M., W. J. Randel, and E. Serrano, 2012: Variability in upwelling across the tropical tropopause and correlations with tracers in the lower stratosphere. *Atmos. Chem. Phys.*, **12**, 11 505–11 517, https://doi.org/10.5194/acp-12-11505-2012.

——, ——, D. E. Kinnison, and E. Serrano, 2013: Quantifying tracer transport in the tropical lower stratosphere using WACCM. *Atmos. Chem. Phys.*, **13**, 10 591–10 607, https://doi.org/10.5194/acp-13-10591-2013.

——, B. Legras, and E. Shuckburgh, 2016a: Interannual variability in effective diffusivity in the upper troposphere/lower stratosphere from reanalysis data. *Quart. J. Roy. Meteor. Soc.*, **142**, 1847–1861, https://doi.org/10.1002/qj.2779.

——, W. J. Randel, and T. Birner, 2016b: Phase-speed spectra of eddy tracer fluxes linked to isentropic stirring and mixing in the upper troposphere and lower stratosphere. *J. Atmos. Sci.*, **73**, 4711–4730, https://doi.org/10.1175/JAS-D-16-0167.1.

Andrews, D. G., J. Holton, and C. B. Leovy, 1987: *Middle Atmosphere Dynamics*. International Geophysics Series, Vol. 40, Academic Press, 489 pp.

Banerjee, A., A. C. Maycock, A. T. Archibald, N. L. Abraham, P. Telford, P. Braesicke, and J. A. Pyle, 2016: Drivers of changes in stratospheric and tropospheric ozone between year 2000 and 2100. *Atmos. Chem. Phys.*, **16**, 2727–2746, https://doi.org/10.5194/acp-16-2727-2016.

Bowman, K. P., and G. D. Carrie, 2002: The mean-meridional transport circulation of the troposphere in an idealized GCM. *J. Atmos. Sci.*, **59**, 1502–1514, https://doi.org/10.1175/1520-0469(2002)059<1502:TMMTCO>2.0.CO;2.

Butchart, N., 2014: The Brewer–Dobson circulation. *Rev. Geophys.*, **52**, 157–184, https://doi.org/10.1002/2013RG000448.

Calvo, N., R. R. Garcia, W. J. Randel, and D. R. Marsh, 2010: Dynamical mechanism for the increase in tropical upwelling in the lowermost tropical stratosphere during warm ENSO events. *J. Atmos. Sci.*, **67**, 2331–2340, https://doi.org/10.1175/2010JAS3433.1.

Chen, G., and A. Plumb, 2014: Effective isentropic diffusivity of tropospheric transport. *J. Atmos. Sci.*, **71**, 3499–3520, https://doi.org/10.1175/JAS-D-13-0333.1.

Erukhimova, T., and K. P. Bowman, 2006: Role of convection in global-scale transport in the troposphere. *J. Geophys. Res.*, **111**, D03105, https://doi.org/10.1029/2005JD006006.

Eyring, V., and Coauthors, 2013: Overview of IGAC/SPARC Chemistry–Climate Model Initiative (CCMI) community simulations in support of upcoming ozone and climate assessments. *SPARC Newsletter*, No. 40, SPARC Office, Zurich, Switzerland, 48–66.

Fang, Y., A. M. Fiore, L. W. Horowitz, A. Gnanadesikan, I. Held, G. Chen, G. Vecchi, and H. Levy, 2011: The impacts of changing transport and precipitation on pollutant distributions in a future climate. *J. Geophys. Res.*, **116**, D18303, https://doi.org/10.1029/2011JD015642.

Forster, P. M. de F., and K. P. Shine, 1997: Radiative forcing and temperature trends from stratospheric ozone changes. *J. Geophys. Res.*, **102**, 10 841–10 855, https://doi.org/10.1029/96JD03510.

——, and ——, 2002: Assessing the climate impact of trends in stratospheric water vapor. *Geophys. Res. Lett.*, **29**, 10-1–10-4, https://doi.org/10.1029/2001GL013909.

Garcia, R. R., and W. J. Randel, 2008: Acceleration of the Brewer–Dobson circulation due to increases in greenhouse gases. *J. Atmos. Sci.*, **65**, 2731–2739, https://doi.org/10.1175/2008JAS2712.1.

——, D. R. Marsh, D. E. Kinnison, B. A. Boville, and F. Sassi, 2007: Simulation of secular trends in the middle atmosphere, 1950–2003. *J. Geophys. Res.*, **112**, D09301, https://doi.org/10.1029/2006JD007485.

——, A. K. Smith, D. E. Kinnison, Á. de la Cámara, and D. J. Murphy, 2017: Modification of the gravity wave parameterization in the Whole Atmosphere Community Climate Model: Motivation and results. *J. Atmos. Sci.*, **74**, 275–291, https://doi.org/10.1175/JAS-D-16-0104.1.

Hall, T. M., and R. A. Plumb, 1994: Age as a diagnostic of stratospheric transport. *J. Geophys. Res.*, **99**, 1059–1070, https://doi.org/10.1029/93JD03192.

Haynes, P., and E. Shuckburgh, 2000: Effective diffusivity as a diagnostic of atmospheric transport: 2. Troposphere and lower stratosphere. *J. Geophys. Res.*, **105**, 22 795, https://doi.org/10.1029/2000JD900092.

Hegglin, M. I., and T. G. Shepherd, 2007: O_3-N_2O correlations from the atmospheric chemistry experiment: Revisiting a diagnostic of transport and chemistry in the stratosphere. *J. Geophys. Res.*, **112**, D19301, https://doi.org/10.1029/2006JD008281.

Held, I. M., and B. J. Soden, 2006: Robust responses of the hydrological cycle to global warming. *J. Climate*, **19**, 5686–5699, https://doi.org/10.1175/JCLI3990.1.

Hess, P. G., 2005: A comparison of two paradigms: The relative global roles of moist convective versus nonconvective transport. *J. Geophys. Res.*, **110**, D20302, https://doi.org/10.1029/2004JD005456.

Holton, J. R., P. H. Haynes, M. E. McIntyre, A. R. Douglass, R. B. Rood, and L. Pfister, 1995: Stratosphere–troposphere

exchange. *Rev. Geophys.*, **33**, 403–439, https://doi.org/10.1029/95RG02097.

Holzer, M., 1999: Analysis of passive tracer transport as modeled by an atmospheric general circulation model. *J. Climate*, **12**, 1659–1684, https://doi.org/10.1175/1520-0442(1999)012<1659:AOPTTA>2.0.CO;2.

——, and G. J. Boer, 2001: Simulated changes in atmospheric transport climate. *J. Climate*, **14**, 4398–4420, https://doi.org/10.1175/1520-0442(2001)014<4398:SCIATC>2.0.CO;2.

Hsu, J., and M. J. Prather, 2014: Is the residual vertical velocity a good proxy for stratosphere–troposphere exchange of ozone? *Geophys. Res. Lett.*, **41**, 9024–9032, https://doi.org/10.1002/2014GL061994.

Johnson, R. H., T. M. Rickenbach, S. A. Rutledge, P. E. Ciesielski, and W. H. Schubert, 1999: Trimodal characteristics of tropical convection. *J. Climate*, **12**, 2397–2418, https://doi.org/10.1175/1520-0442(1999)012<2397:TCOTC>2.0.CO;2.

Kawatani, Y., and K. Hamilton, 2013: Weakened stratospheric quasibiennial oscillation driven by increased tropical mean upwelling. *Nature*, **497**, 478–481, https://doi.org/10.1038/nature12140.

Kinnison, D. E., and Coauthors, 2007: Sensitivity of chemical tracers to meteorological parameters in the MOZART-3 chemical transport model. *J. Geophys. Res.*, **112**, D20302, https://doi.org/10.1029/2006JD007879.

Lauritzen, P. H., P. A. Ullrich, and R. D. Nair, 2011: Atmospheric transport schemes: Desirable properties and a semi-Lagrangian view on finite-volume discretizations. *Numer. Tech. Global Atmos. Models*, **80**, 185–250, https://doi.org/10.1007/978-3-642-11640-7_8.

Lin, S.-J., 2004: A vertically Lagrangian finite-volume dynamical core for global models. *Mon. Wea. Rev.*, **132**, 2293–2307, https://doi.org/10.1175/1520-0493(2004)132<2293:AVLFDC>2.0.CO;2.

Lorenz, D. J., and E. T. DeWeaver, 2007: Tropopause height and zonal wind response to global warming in the IPCC scenario integrations. *J. Geophys. Res.*, **112**, D10119, https://doi.org/10.1029/2006JD008087.

Mahlman, S. D., and W. J. Moxim, 1978: Tracer simulation using a global general circulation model: Results from a midlatitude instantaneous source experiment. *J. Atmos. Sci.*, **35**, 1340–1374, https://doi.org/10.1175/1520-0469(1978)035<1340:TSUAGG>2.0.CO;2.

Marsh, D. R., M. J. Mills, D. E. Kinnison, J. F. Lamarque, N. Calvo, and L. M. Polvani, 2013: Climate change from 1850 to 2005 simulated in CESM1(WACCM). *J. Climate*, **26**, 7372–7391, https://doi.org/10.1175/JCLI-D-12-00558.1.

——, J. F. Lamarque, A. J. Conley, and L. M. Polvani, 2016: Stratospheric ozone chemistry feedbacks are not critical for the determination of climate sensitivity in CESM1(WACCM). *Geophys. Res. Lett.*, **43**, 3928–3934, https://doi.org/10.1002/2016GL068344.

Matsuno, T., 1970: Vertical propagation of stationary planetary waves in the winter Northern Hemisphere. *J. Atmos. Sci.*, **27**, 871–883, https://doi.org/10.1175/1520-0469(1970)027<0871:VPOSPW>2.0.CO;2.

Maycock, A. C., M. M. Joshi, K. P. Shine, S. M. Davis, and K. H. Rosenlof, 2014: The potential impact of changes in lower stratospheric water vapour on stratospheric temperatures over the past 30 years. *Quart. J. Roy. Meteor. Soc.*, **140**, 2176–2185, https://doi.org/10.1002/qj.2287.

Morgenstern, O., and Coauthors, 2017: Review of the global models used within phase 1 of the Chemistry–Climate Model Initiative (CCMI). *Geosci. Model Dev.*, **10**, 639–671, https://doi.org/10.5194/gmd-2016-199.

Mote, P. W., and Coauthors, 1996: An atmospheric tape recorder: The imprint of tropical tropopause temperatures on stratospheric water vapor. *J. Geophys. Res.*, **101**, 3989–4006, https://doi.org/10.1029/95JD03422.

Nakamura, N., 1996: Two-dimensional mixing, edge formation, and permeability diagnosed in an area coordinate. *J. Atmos. Sci.*, **53**, 1524–1537, https://doi.org/10.1175/1520-0469(1996)053<1524:TDMEFA>2.0.CO;2.

Neale, R. B., J. Richter, S. Park, P. H. Lauritzen, S. J. Vavrus, P. J. Rasch, and M. Zhang, 2013: The mean climate of the Community Atmosphere Model (CAM4) in forced SST and fully coupled experiments. *J. Climate*, **26**, 5150–5168, https://doi.org/10.1175/JCLI-D-12-00236.1.

Neu, J. L., T. Flury, G. L. Manney, M. L. Santee, N. J. Livesey, and J. Worden, 2014: Tropospheric ozone variations governed by changes in stratospheric circulation. *Nat. Geosci.*, **7**, 340–344, https://doi.org/10.1038/ngeo2138.

Nowack, P. J., N. Luke Abraham, A. C. Maycock, P. Braesicke, J. M. Gregory, M. M. Joshi, A. Osprey, and J. Pyle, 2014: A large ozone-circulation feedback and its implications for global warming assessments. *Nat. Climate Change*, **5**, 41–45, https://doi.org/10.1038/nclimate2451.

Oberländer-Hayn, S., and Coauthors, 2016: Is the Brewer–Dobson circulation increasing or moving upward? *Geophys. Res. Lett.*, **43**, 1772–1779, https://doi.org/10.1002/2015GL067545.

Oman, L. D., A. R. Douglass, J. R. Ziemke, J. M. Rodriguez, D. W. Waugh, and J. E. Nielsen, 2013: The ozone response to ENSO in Aura satellite measurements and a chemistry–climate simulation. *J. Geophys. Res. Atmos.*, **118**, 965–976, https://doi.org/10.1029/2012JD018546.

Orbe, C., M. Holzer, L. M. Polvani, and D. Waugh, 2013: Air-mass origin as a diagnostic of tropospheric transport. *J. Geophys. Res. Atmos.*, **118**, 1459–1470, https://doi.org/10.1002/jgrd.50133 .

——, D. W. Waugh, H. Yang, J.-F. Lamarque, S. Tilmes, and D. E. Kinnison, 2017: Tropospheric transport differences between models using the same large-scale meteorological fields. *Geophys. Res. Lett.*, **44**, 1068–1078, https://doi.org/10.1002/2016GL071339.

Pan, L. L., S. B. Honomichl, D. E. Kinnison, M. Abalos, W. J. Randel, J. W. Bergman, and J. Bian, 2016: Transport of chemical tracers from the boundary layer to stratosphere associated with the dynamics of the Asian summer monsoon. *J. Geophys. Res. Atmos.*, **121**, 14 159–14 174, https://doi.org/10.1002/2016JD025616.

Ploeger, F., and T. Birner, 2016: Seasonal and interannual variability of lower stratospheric age of air spectra. *Atmos. Chem. Phys.*, **16**, 10 195–10 213, https://doi.org/10.5194/acp-16-10195-2016.

——, and Coauthors, 2012: Horizontal transport affecting trace gas seasonality in the Tropical Tropopause Layer (TTL). *J. Geophys. Res.*, **117**, D09303, https://doi.org/10.1029/2011JD017267.

——, and Coauthors, 2013: Horizontal water vapor transport in the lower stratosphere from subtropics to high latitudes during boreal summer. *J. Geophys. Res. Atmos.*, **118**, 8111–8127, https://doi.org/10.1002/jgrd.50636.

——, M. Abalos, T. Birner, P. Konopka, B. Legras, R. Mller, and M. Riese, 2015: Quantifying the effects of mixing and residual circulation on trends of stratospheric mean age of air. *Geophys. Res. Lett.*, **42**, 2047–2054, https://doi.org/10.1002/2014GL062927.

Plumb, R. A., 2002: Stratospheric transport. *J. Meteor. Soc. Japan*, **80**, 793–809, https://doi.org/10.2151/jmsj.80.793.

——, and J. D. Mahlman, 1987: The zonally averaged transport characteristics of the GFDL general circulation/transport model. *J. Atmos. Sci.*, **44**, 298–327, https://doi.org/10.1175/1520-0469(1987)044<0298:TZATCO>2.0.CO;2.

Prather, M. J., X. Zhu, Q. Tang, J. Hsu, and J. L. Neu, 2011: An atmospheric chemist in search of the tropopause. *J. Geophys. Res.*, **116**, D04306, https://doi.org/10.1029/2010JD014939.

Randel, W. J., B. A. Boville, J. C. Gille, P. L. Bailey, S. T. Massie, J. B. Kumer, J. L. Mergenthaler, and A. E. Roche, 1994: Simulation of stratospheric N_2O in the NCAR CCM2: Comparison with CLAES data and global budget analyses. *J. Atmos. Sci.*, **51**, 2834–2845, https://doi.org/10.1175/1520-0469(1994)051<2834:SOSNIT>2.0.CO;2.

——, F. Wu, S. J. Oltmans, K. Rosenlof, and G. E. Nedoluha, 2004: Interannual changes of stratospheric water vapor and correlations with tropical tropopause temperatures. *J. Atmos. Sci.*, **61**, 2133–2148, https://doi.org/10.1175/1520-0469(2004)061<2133:ICOSWV>2.0.CO;2.

——, M. Park, F. Wu, and N. Livesey, 2007: A large annual cycle in ozone above the tropical tropopause linked to the Brewer–Dobson circulation. *J. Atmos. Sci.*, **64**, 4479–4488, https://doi.org/10.1175/2007JAS2409.1.

——, R. R. Garcia, N. Calvo, and D. Marsh, 2009: ENSO influence on zonal mean temperature and ozone in the tropical lower stratosphere. *Geophys. Res. Lett.*, **36**, L15822, https://doi.org/10.1029/2009GL039343.

——, L. Rivoire, L. L. Pan, and S. B. Honomichl, 2016: Dry layers in the tropical troposphere observed during CONTRAST and global behavior from GFS analyses. *J. Geophys. Res. Atmos.*, **121**, 14 142–14 158, https://doi.org/10.1002/2016JD025841.

Ray, E. A., F. L. Moore, K. H. Rosenlof, D. A. Plummer, F. Kolonjari, and K. A. Walker, 2016: An idealized stratospheric model useful for understanding differences between long-lived trace gas measurements and global chemistry–climate model output. *J. Geophys. Res. Atmos.*, **121**, 5356–5367, https://doi.org/10.1002/2015JD024447.

Richter, J. H., F. Sassi, and R. R. Garcia, 2010: Toward a physically based gravity wave source parameterization in a general circulation model. *J. Atmos. Sci.*, **67**, 136–156, https://doi.org/10.1175/2009JAS3112.1.

Rind, D., J. Lerner, and C. McLinden, 2001: Changes of tracer distributions in the doubled CO_2 climate. *J. Geophys. Res.*, **106**, 28 061–28 079, https://doi.org/10.1029/2001JD000439.

Shepherd, T. G., and C. McLandress, 2011: A robust mechanism for strengthening of the Brewer–Dobson circulation in response to climate change: Critical-layer control of subtropical wave breaking. *J. Atmos. Sci.*, **68**, 784–797, https://doi.org/10.1175/2010JAS3608.1.

Solomon, S., K. H. Rosenlof, R. W. Portmann, J. S. Daniel, S. M. Davis, T. J. Sanford, and G.-K. Plattner, 2010: Contributions of stratospheric water vapor to decadal changes in the rate of global warming. *Science*, **327**, 1219–1223, https://doi.org/10.1126/science.1182488.

Stohl, A., and Coauthors, 2003: Stratosphere–troposphere exchange: A review, and what we have learned from STACCATO. *J. Geophys. Res.*, **108**, 8516, https://doi.org/10.1029/2002JD002490.

Trenberth, K. E., 1997: The definition of El Niño. *Bull. Amer. Meteor. Soc.*, **78**, 2771–2777, https://doi.org/10.1175/1520-0477(1997)078<2771:TDOENO>2.0.CO;2.

Vallis, G. K., P. Zurita-Gotor, C. Cairns, and J. Kidston, 2015: Response of the large-scale structure of the atmosphere to global warming. *Quart. J. Roy. Meteor. Soc.*, **141**, 1479–1501, https://doi.org/10.1002/qj.2456.

von Storch, H., and F. W. Zwiers, 2002: *Statistical Analysis in Climate Research.* Cambridge University Press, 496 pp.

Wallace, J. M., R. L. Panetta, and J. Estberg, 1993: Representation of the equatorial stratospheric quasi-biennial oscillation in EOF phase space. *J. Atmos. Sci.*, **50**, 1751–1762, https://doi.org/10.1175/1520-0469(1993)050<1751:ROTESQ>2.0.CO;2.

Waugh, D., and T. M. Hall, 2002: Age of stratospheric air: Theory, observations, and models. *Rev. Geophys.*, **40**, 1-1–1-26, https://doi.org/10.1029/2000RG000101.

Yang, H., G. Chen, Q. Tang, and P. Hess, 2016: Quantifying isentropic stratosphere–troposphere exchange of ozone. *J. Geophys. Res. Oceans*, **121**, 4928–4945, https://doi.org/10.1002/2015JC011513.